CrossMark

X-Ray Reprocessing: Through the Eclipse Spectra of High-mass X-Ray Binaries with *XMM-Newton*

Nafisa Aftab[1], Biswajit Paul[1], and Peter Kretschmar[2]
[1] Raman Research Institute, C V Raman Avenue, Sadashivanagar, Bangalore 560080, India; nafisa@rri.res.in, aftabnafisa@gmail.com
[2] European Space Agency European Space Astronomy Center (ESA-ESAC), Camino Bajo del Castillo, s/n., Urb. Villafranca del Castillo, E-28692 Villanueva de la Cañada, Madrid, Spain

Abstract

The study of X-ray reprocessing is one of the key diagnostic tools to probe the environment in X-ray binary systems. One difficult aspect of studying X-ray reprocessing is the presence of much brighter primary radiation from the compact star together with the reprocessed radiation. In contrast, for eclipsing systems, the X-rays we receive during eclipse are only those produced by the reprocessing of the emission from the compact star by the surrounding medium. We report results from a spectral study of the X-ray emission during eclipse and outside eclipse in nine high-mass X-ray binaries (HMXBs) with the *XMM-Newton* European Photon Imaging Camera (EPIC) pn to investigate different aspects of the stellar wind in these HMXBs. During eclipse the continuum component of the spectrum is reduced by a factor of $\sim$8–237, but the count rate for the 6.4 keV iron emission line or the complex of iron emission lines in HMXBs is reduced by a smaller factor, leading to large equivalent widths of the iron emission lines. This indicates a large size for the line emission region, comparable to or larger than the companion star in these HMXB systems. However, there are significant system to system differences. 4U 1538 $-$522, despite having a large absorption column density, shows a soft emission component with comparable flux during the eclipse and out-of-eclipse phases. Emission from hydrogen-like iron has been observed in LMC X-4 for the first time, in the out-of-eclipse phase in one of the observations.. Overall, we find significant differences in the eclipse spectrum of different HMXBs and also in their eclipse spectra against out-of-eclipse spectra.

Key words: binaries: eclipsing – stars: neutron – supergiants

1. Introduction

In X-ray binary systems, the X-rays produced very close to the compact object fueled by accretion are called primary X-rays. Usually, a large fraction of these X-rays escapes directly from the system and can be directly observed. But a significant fraction interacts with the matter surrounding the compact object and are re-emitted. This emission is called secondary emission. Depending on the interaction of the primary X-rays with the surrounding matter, the secondary photons can have a wide range of energies. This phenomenon is known as the reprocessing of X-rays (or X-ray reprocessing). The secondary emission as a whole is called reprocessed emission, and the secondary X-rays are known as reprocessed X-rays.

Low-energy primary X-rays colliding with very low-energy electrons through Thomson scattering are reflected at the same energy they had before the interaction. Higher energy X-rays can interact with lower energy electrons, giving off some of their energy to the electrons via Compton scattering and coming out as lower energy X-rays, UV, or optical photons. Moderate energy X-ray photons can be upscattered by relativistic electrons of the hot plasma and gain energy. Some X-rays interact with ionized or neutral atoms, excite electrons, and give rise to different spectral lines in the X-ray, UV, or optical bands. X-ray photons can be absorbed by the photoionization of neutral or ionized atoms, leading to reemission of photons at lower energies. Photons can also be

affected by gravitational redshift. Reprocessing of X-rays is ubiquitous and has been observed in systems with accreting black holes, neutron stars,and white dwarfs, and in active galactic nuclei (AGNs).

The X-ray reprocessing characteristics as seen from Earth depend on several factors, for example, (1) the density and distribution of matter around the accretor, (2) structures in an accretion disk, if one is present, (3) the orbital phase of the system, (4) the chemical composition and ionization levels of the matter in the system, and (5) the viewing angle of the observer. X-ray reprocessing has proven to be a very useful tool in unveiling the geometry, distribution of matter and its ionization level, and also the mechanisms of accreting systems.

There have been theoretical and observational studies of X-ray reprocessing, starting from AGNs to low-mass X-ray binary (LMXB) systems, which have revealed different unique features of these systems: AGNs—Zycki et al. (1994); LMXBs—de Jong et al. (1996); Seyfert galaxy NGC 2992—Weaver et al. (1996); supersoft X-ray source (SSS) CAL 87 (cataclysmic variable)—Suleimanov et al. (2003); black hole binary XTE J1817$-$330—Gierliński et al. (2009), etc.

In this work, we focus on the X-ray reprocessing in high-mass X-ray binary (HMXB) systems. In HMXB systems ,the companion star is a high-mass star ($\geqslant$10 $M_\odot$), either a main-sequence star or a supergiant, and the compact object is either a neutron star or a black hole. In HMXB systems with a supergiant companion (SgHMXB system), most of the time the compact object is embedded in the dense wind of the companion star, so the primary X-rays encounter scattering in these systems, which results in reprocessing. Often, the supergiant's wind contains clumps of different densities and sizes, and intraclump regions are filled with rarefied wind

materials (Oskinova et al. 2013). The reverse scenario is also possible, i.e., there could be lower density zones in a dense ambient medium. This causes a variation of the X-ray reprocessing with the distribution of matter around the compact object. Supergiant fast X-ray transients (SFXTs) are a newer class of SgHMXBs (Sguera et al. 2005; Negueruela et al. 2006), which are usually dim sources (average luminosity 10^{33}–$10^{34}\,\mathrm{erg\,s^{-1}}$), but often appear with unpredicted intense flares (with flare luminosity reaching 10^{36}–$10^{37}\,\mathrm{erg\,s^{-1}}$). However, most of the time, the SFXTs have X-ray luminosity that is 3–4 orders of magnitude fainter compared to that of classical HMXBs (luminosity at quiescent $10^{32}\,\mathrm{erg\,s^{-1}}$). These drastic changes of luminosities in SFXTs indicate a quite dynamic accretion scenario in these systems, and hence variable wind structures around the compact object or a different interaction between the compact object and the companion's wind. In both cases, a large variation in the X-ray reprocessing is expected. Accretion disks exist in some HMXB systems (Cen X-3, LMC X-4, SMC X-1: Savonije 1978; van der Meer et al. 2007). Frequently, structures (warps) form and decay in the accretion disk. The structures can differ in density, temperature, shape, etc., and have different solid angles to the primary X-rays. Moreover, these structures evolve with time, causing variation in the X-ray reprocessing.

Analyzing reprocessed X-ray emissions, we can derive clues about the environment of the compact object in an X-ray binary system. But the difficult aspect of studying reprocessed X-rays in X-ray binary systems is that the reprocessed emission is detected along with the primary emission from the compact object, which is much brighter. During eclipse, the primary X-rays are blocked by the companion, and the X-rays we receive are the reprocessed X-rays only. The intensity of the reprocessed X-rays is expected to be smaller by a factor of a few. This increases the equivalent width of a spectral line, when the emitting material is distributed in an extended region. Thus, the detection of a spectral line becomes more significant during an eclipse. These spectral lines give useful information about the chemical composition and ionization state of matter around the compact object. When the compact object is not in eclipse, then the line intensity may be less significant compared to the continuum and therefore difficult to measure accurately (if the line intensity itself is not very intense). This results in low equivalent width, and the line detection becomes less significant out-of-eclipse. The comparison of equivalent widths during eclipse can give useful insight into the distribution of different matter in different binary systems and in a binary system at different epochs, in much more efficient way compared to the out-of-eclipse phase.

Eclipse spectra of individual sources have been reported before (Cen X-3—Ebisawa et al. 1996, Wojdowski et al. 2001, Naik & Paul 2012; 4U 1538−522—Rodes-Roca et al. 2011; 4U 1700 −377—van der Meer et al. 2005; Vela X-1—Sako et al. 1999, Schulz et al. 2002). The scattered reports on individual sources do not give an overall picture of the extent of reprocessing during eclipse in HMXBs, i.e., what the fractional luminosity compared to the out-of-eclipse spectrum is, how the shape of the continuum during the eclipse compares with that in the out-of-eclipse spectrum, and the relative strength of the iron (Fe) fluorescence line and other Fe lines if present. Moreover, we also aim to study system to system variability and possible dependencies on the type, mass, or mass-loss rate of the companion, and also to investigate the stability of the reprocessing in a given source

when multiple data sets exist. There indeed exists a large number of papers that investigate or use reprocessing as a tool, but this is the first work on a comprehensive analysis of all available eclipse data of HMXB systems with the *XMM-Newton* European Photon Imaging Camera (EPIC) pn, an instrument particularly suitable owing to its large collection area and CCD spectral resolution for the study of isolated emission lines.

Out of 15 eclipsing HMXBs, nine sources were observed with *XMM-Newton*. In this work, we analyzed all available observations of HMXBs that include eclipses with *XMM-Newton* EPIC pn: in seven supergiant HMXBs or SgHMXBs (Cen X-3, 4U 1700−377, 4U 1538−522, SMC X-1, LMC X-4, IGR J18027−2016, IGR J17252−3616) and in two SFXTs namely IGR J16479−4514 and IGR J16418−4532. We focused on these observations in order to have a coherent data sample for analysis and comparison. A list of the important parameters of these sources is given in Table 1. In the following paragraph, we discuss some of the observed features of these systems that are relevant to our analysis.

Cen X-3 was the first discovered X-ray binary pulsar (Giacconi et al. 1971) that accretes matter directly from the supergiant's wind and also through disk accretion via Roche lobe overflow (Nagase et al. 1992; Day & Stevens 1993). Nagase et al. (1992) observed an Fe line in Cen X-3 with energy ~6.5 keV. The intensity of this line was observed to be pulsating with phase, which indicates that the matter surrounding the neutron star causing this fluorescent line is not uniformly distributed (Day & Stevens 1993). Ebisawa et al. (1996), using 1993 ASCA observations, clearly resolved three Fe K_α emission lines with energies of 6.4, 6.7, and 6.97 keV during eclipse. The highly ionized 6.7 and 6.97 keV emission lines could not be resolved in the pre-eclipse phase. The line parameters indicate that the origin of the fluorescent 6.4 keV line was closer to the neutron star compared to that of the highly ionized Fe K_α emission lines. Del Sordo et al. (2000) investigated two *BeppoSAX* observations of Cen X-3 in 1996 August and in 1997 February. They found significantly a higher energy of the fluorescent Fe K_α emission line (~6.6 keV), which could be a blend of the 6.4 keV emission line with the 6.7 keV emission line originating from the hot matter surrounding the neutron star. Naik & Paul (2012), using the same *XMM-Newton* observation we analyzed here, found significant variability in the line parameters of the three Fe K_α emission lines during the eclipse and out-of-eclipse phases. They also suggest that the colder material causing the 6.4 keV line emission is relatively close to the neutron star, at most on the scale of the companion, while the hot matter producing the Fe XXV and Fe XXVI emission lines are farther away, as suggested by Ebisawa et al. (1996). A cyclotron resonance-scattering feature at 28 and 30 keV was detected in Cen X-3 with two *BeppoSAX* observations (Santangelo et al. 1998; Burderi et al. 2000). A *Suzaku* observation of Cen X-3 covering a full binary orbit showed multiple extended dips with spectral characteristics similar to that of the source in eclipse, indicating that the dips are produced by the obscuration of dense matter, which are structures in the outer region of the accretion disk (Naik et al. 2011).

LMC X-4 is a wind- and disk-fed persistent system in the Large Magellanic Cloud (LMC), which often shows X-ray flares sometimes with super-Eddington luminosity (Levine et al. 2000; Moon et al. 2003). The source was found to show periodicity longer than the orbital period, called the superorbital period, of

Table 1
List of Basic Parameters of the Eclipsing HMXBs Analyzed in This Work

Source	Mode of Accretion	P_{orb}	M_C	R_C	S_C	e	a	$\dot{M}_w$	d
Cen X-3	wind+disk (a1)	2.09 (a2)	(20.5 ± 0.7) (a3)	12.1 ± 0.5 (a4)	O6.5 II-III (a4)	⩽ 0.0016 (a5)	39.6612 ± 0.0009 (a6)	5.3 (a1)	5.7 ± 1.5 (a7)
LMC X-4	wind+disk (a1)	1.41 (b2)	$14.5^{+1.1}_{-1.0}$ (a4)	$7.8^{+0.3}_{-0.4}$ (a4)	O8 III (a4)	0.0006 ± 0.0002 (b3)	26.343 ± 0.016 (b3)	2.4 (a1)	49.97 ± 0.19 ± 1.11 (b4)
SMC X-1	wind+disk (a1)	3.89 (c2)	(16.6 ± 0.4) (c3)	18 (c4)	B0 I (c5)	<0.0007 (c4)	53.4876 lt-s (c6)	15 (a1)	60.6 ± 1.0 ± 2.8 (c7)
4U 1700−377	wind (a1)	3. 412 (d1)	(52 ± 2) (d2)	$21.9^{+1.3}_{-0.5}$ (d2)	O7f (d3)	<0.008 (d4)	48–82 (d1)	>21 (a1)	1.8 (d5)
4U 1538−522	wind (a1)	3.75 (e2)	(19.9 ± 3.4) (e3)	17.2 ± 1.0 (e3)	B0Iab (e4)	0.174 ± 0.015 (e5)	53.1 ± 1.5 (e5)	8.3 (a1)	6.4 ± 1.0 (e5)
IGR J18027−2016	wind (a1)	4.56 (f2)	18.8–29.3 (f2)	(15.0–23.4) (f2)	B1-Ib (f3)	6.3 (f1b)	68 ± 1 (f2)	6.3 (a1)	...
IGR J17252−3616	wind (a1)	9.74 (i2)	15 (i3)	21–37 (i2)	B0 I–B5 I (i2)	<0.19 (i2)	101 ± 3 (i2)	9.0 (a1)	5.3–8.7 (i2)
IGR J16479−4514	SFXT (g0), (g1)	3.32 (g2)	30 (g3)	23.8 (g3)	O9.5 Iab (g4)	...	(44.85–48.90) (z1)	(10–70) (y2)	$2.8^{+4.9}_{-1.7}$ (g4)
IGR J16418−4532	SFXT (h0)	3.75 (h2)	31.54 (h3)	21.41 (h3)	BN 0.5 Ia (h4)	...	(48.65–53.03) (z2)	(2.3–3.8) (y3)	13 (h5)

Note. P_{orb}: orbital period (days), M_C: mass of the companion ($M_\odot$), R_C: radius of the companion star ($R_\odot$), S_C: spectral type of the companion, e: eccentricity of the HMXB orbit, a: length of the semimajor axis of the system ($a_x \sin i$ [light-second]), $\dot{M}_w$: mass-loss rate of the companion star ($10^{-7} M_\odot yr^{-1}$), and d: distance from Earth (kpc). ($M_\odot$, $R_\odot$: mass and radius of the Sun, respectively). (a1) Falanga et al. (2015), (a2) Schreier et al. (1972b), (a3) Ash et al. (1999), (a4) van der Meer et al. (2007), (a5) Bildsten et al. (1997), (a6) Raichur & Paul (2010), (a7) Thompson & Rothschild (2009), (b2) Li et al. (1978); White (1978), (b3) Levine et al. (2000), (b4) Pietrzyński et al. (2013), (c2) Schreier et al. (1972a), (c3) Val Baker et al. (2005), (c4) Primini et al. (1977), (c5) Reynolds et al. (1993), (c6) Levine et al. (1993), (c7) Hilditch et al. (2005), (d1) Jones et al. (1973), (d2) Clark et al. (2002), (d3) Penny et al. (1973), (d4) Islam & Paul (2016), (d5) Ankay et al. (2001), (e2) Becker et al. (1977), (e3) Reynolds et al. (1992), (e4) Parkes et al. (1978), Falanga et al. (2015), (e5) Mukherjee et al. (2006), (f1b) Augello et al. (2003), (f2) Hill et al. (2005), Jain et al. (2009b), (f3) Torrejón et al. (2010a), (g0) Sguera et al. (2005), (g1) Molkov et al. (2003), (g2) Jain et al. (2009a), (g3) Vacca et al. (1996), (g4) Nespoli et al. (2008), (h0) Romano et al. (2011), (h2) Corbet et al. (2006), (h3) Martins et al. (2005), (h4) Coleiro et al. (2013), (i2) Thompson et al. (2007), (i3) Takeuchi et al. (1990), (y2) Sidoli et al. (2012b), (y3) Drave et al. (2013b), (z1), (z2) Derived from the total mass of the binary and the orbital period, taken from Coley et al. (2015).

30.5 days (Lang et al. 1981). The pulsation of the soft spectral component and the power-law component showed significant phase differences with *ROSAT*, *GINGA*, *ASCA*, *BeppoSAX*, and the *XMM-Newton* and *Suzaku* observatories (Woo et al. 1996; Paul & Kitamoto 2002; Naik & Paul 2004b; Hung et al. 2010; Beri & Paul 2017). These indicate different origins of the soft and hard X-rays. LMC X-4 shows short super-Eddington bursts, during which the pulse profile of the pulsar changes both in phase and shape. The same has been observed with *RXTE*-PCA (Levine et al. 2000), *XMM-Newton* (Beri & Paul 2017), and *NuStar* (Shtykovsky et al. 2018).

SMC X-1 is a wind- and disk-fed binary pulsar located in the Small Magellanic Cloud (SMC), which has been observed at both sub-Eddington and super-Eddington luminosities and shows short and intense bursts like LMC X-4 (Price et al. 1971; Ulmer et al. 1973; Coe et al. 1981). It has a highly variable superorbital period (between ~40 and 65 days; Hu et al. 2013). *ROSAT*, *GINGA*, and *ASCA* observations of the source show an out-of-eclipse flux variation of a factor of 20 between the high and low states while eclipsed flux and spectral parameters remain nearly the same in both states. This possibly indicates the blocking of the neutron star's direct emission by a precessing tilted accretion disk (Wojdowski et al. 1998). Observations of SMC X-1 were carried out at different superorbital phases with *Chandra* and *XMM-Newton* to investigate the case of a precessing warped accretion disk in this source (Hickox & Vrtilek 2005). Broadband spectroscopy of SMC X-1 carried out with multiple *Suzaku* (Kubota et al. 2018) and *NuStar* (Pike et al. 2019) observations have reinforced the same.

4U 1700−377 is an HMXB wind-fed system for which the nature of the compact object is not yet clear. The source has been observed with pronounced variability with strong flares, which is believed to be due to accretion from the supergiant's inhomogeneous wind (White et al. 1983). van der Meer et al. (2005) detected several recombination and fluorescent lines including highly ionized and fluorescent Fe K_α emission lines in the eclipse and eclipse egress and in low-flux *XMM-Newton* spectra, where lines are most prominent during eclipse. They suggested that extended ionized plasma surrounds the compact object. Jaisawal & Naik (2015) found 6.4 keV Fe K_α and 7.1 keV Fe K_β emission lines in 20 time-resolved out-of-eclipse *Suzaku* spectra of the source. The relation between the flux and equivalent width of these Fe emission lines indicates that these lines originate from the matter near the compact object. They found a significant increase of the line-of-sight equivalent hydrogen column density during low-flux out-of-eclipse phases, indicating an inhomogeneous distribution of the wind.

4U 1538−522 is a wind-fed X-ray binary pulsar. Rodes-Roca et al. (2011) analyzed its eclipse and phase-average out-of-eclipse spectra with *XMM-Newton*. They found Fe emission lines in the energy range of 6–7 keV and several recombination lines below 3 keV in the eclipse spectrum. These indicate the presence of emitting material over a large distance comparable to or greater than the size of the supergiant companion. Mukherjee et al. (2006) detected a 6.4 keV Fe emission line with *RXTE* and *BeppoSAX*. They found varying line-of-sight equivalent hydrogen column densities over the orbital phase, which asymmetrically increases before and after the eclipse. This indicates a trailing accretion stream or wakes from the supergiant companion. A cyclotron resonance-scattering feature at around 22 keV was observed in 4U 1538−522 in detail

with *Suzaku* (Hemphill et al. 2014), *AstroSat* (Varun et al. 2019), and *NuStar* (Hemphill et al. 2019).

IGR J18027−2016 is a wind-fed HMXB pulsar. *INTEGRAL* and *XMM-Newton* observations of the source show a high value of the line-of-sight hydrogen column density, which indicates intrinsic absorption (Hill et al. 2005). Aftab et al. (2016) found several low-intensity states in the source with Swift–XRT, while *Swift*-BAT shows a smooth variation over the orbit. They also found a high value of the line-of-sight hydrogen column density, which actually increases before and after the eclipse. These indicate an accreting trailing wind from the supergiant companion to the pulsar crossing the line of sight like in 4U 1538−522. A cyclotron resonance-scattering feature at 23 keV has been discovered in IGR J18027−2016 with *NuStar* (Lutovinov et al. 2017).

IGR J17252−3616 is a wind-fed X-ray binary pulsar showing strong X-ray absorption (Tawara et al. 1989; Walter et al. 2004). Thompson et al. (2007) obtained orbital phase-resolved spectroscopy with *RXTE*. They found variations in flux, line-of-sight equivalent hydrogen column density, photon index, and Fe line equivalent width. Column densities rise by a factor of $\geqslant 10$ just before the eclipse ingress and after the egress; this indicates a spherically symmetric wind outflow from the supergiant, which is trailing the pulsar in its orbit.

IGR J16479−4514 and IGRJ 16418−4532 are SFXTs discovered with *INTEGRAL* in 2003 (Sguera et al. 2005; Negueruela et al. 2006). IGR J16479−4514 showed more frequent X-ray outbursts than other SFXTs in the past (Walter & Zurita Heras 2007). It is the SFXT with the smallest orbital period, 3.32 days (Jain et al. 2009a). Accretion onto the compact object is very likely from the supergiant's wind (Romano et al. 2008). The X-ray emission from the source was observed to be highly variable on timescales of seconds to weeks during outbursts and in quiescence (Sidoli et al. 2008). The occurrence of flares in similar orbital phases suggests a phase-locked wind structure in the system (Bozzo et al. 2009; Sidoli et al. 2013). IGR J16418−4532 is a heavily absorbed pulsar as observed with *INTEGRAL* (Walter et al. 2006). A superorbital modulation has been observed in the source (Corbet & Krimm 2013; Drave et al. 2013a). It is an intermediate accretor, between pure wind accretion and full Roche lobe overflow (Sidoli et al. 2012a). Drave et al.'s (2013b) analysis of *XMM-Newton* data suggests clumpy wind structures of the supergiant's wind.

We also analyzed the out-of-eclipse spectra, whenever available, in the same observation along with the eclipse. We try to infer the X-ray wind characteristics of these systems, which is the main reprocessing agent in the HMXBs.

2. Observation and Data Analysis

XMM-Newton was launched in 1999 December. The X-ray observatory consists of three sets of coaligned X-ray telescopes, each with an effective area of 1500 cm^2 with the following focal plane instruments: three EPIC and two Reflection Grating Spectrometers (RGS). Two of the cameras are made of Metal Oxide Semi-conductor (MOS) CCD (Turner et al. 2001) arrays and one uses pn CCD (Strüder et al. 2001). The pn camera is placed at the focal plane of one telescope and the two MOS cameras along with the RGS are placed at the focal plane of the other two telescopes. There is one coaligned Optical/UV Monitor (OM) telescope (Mason et al. 2001),
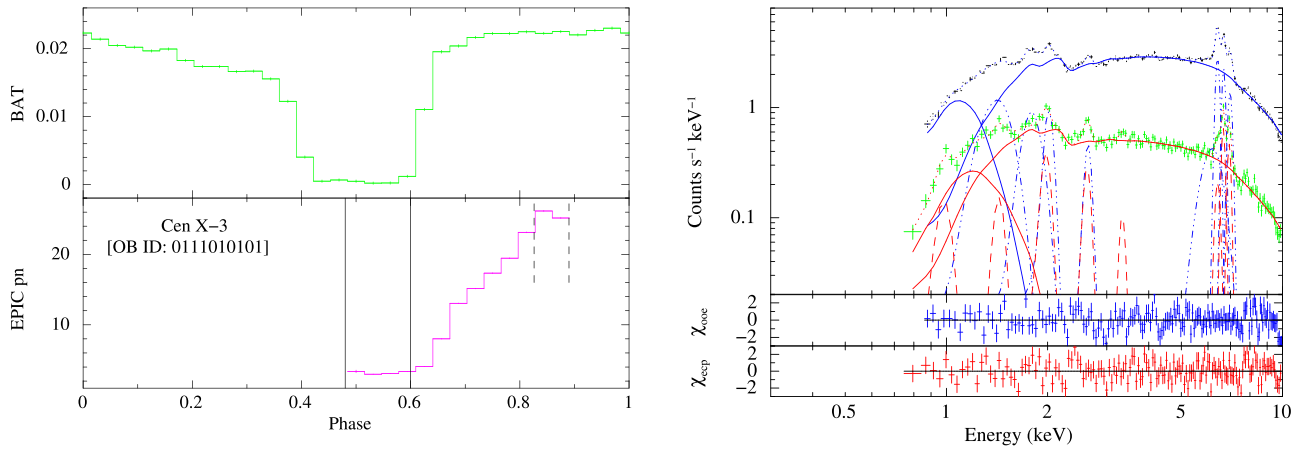
Figure 1. Left figure: the top panel shows the long-term average BAT orbital profile of Cen X-3 and the bottom panel shows EPIC pn light curve of Cen X-3 (OBS ID: 0111010101) folded with its orbital period. The eclipse spectrum and the out-of-eclipse spectrum were extracted from the duration shown with the solid and dashed lines, respectively. Right figure: the top panel gives the EPIC pn out-of-eclipse and the eclipse spectrum of Cen X-3, where data points for the out-of-eclipse spectrum are plotted in black and those for the eclipse spectrum are plotted in green. Model components of the out-of-eclipse and the eclipse spectrum are shown in blue and red, respectively. The emission lines for the out-of-eclipse spectrum are shown with blue lines and those for the eclipse spectrum are shown with red lines. The middle and bottom panels show the contribution of each bin toward χ for the best-fit spectral model for the out-of-eclipse spectrum and the eclipse spectrum, respectively.
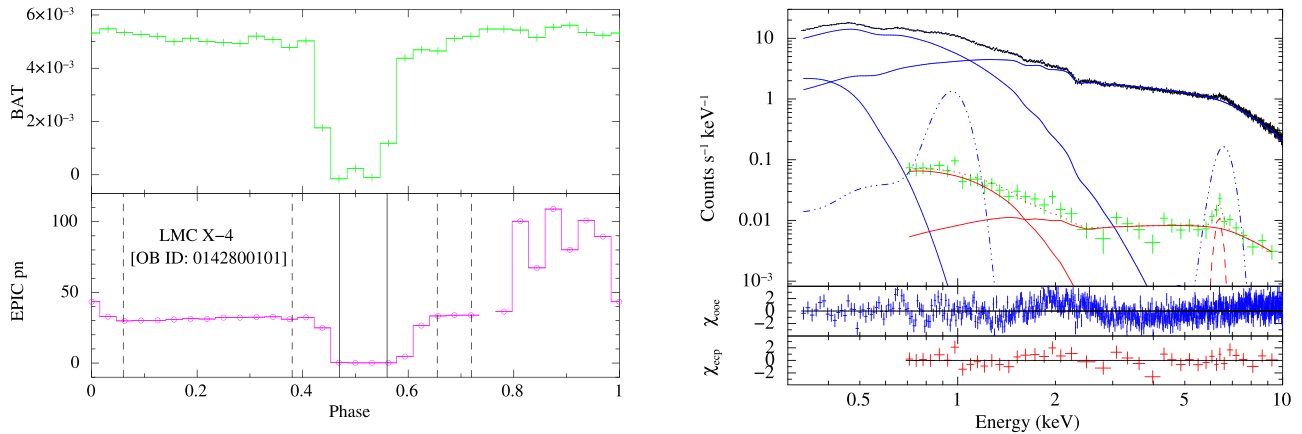

Figure 2. Same as Figure 1 for LMC X-4 (OBS ID: 0142800101).

which provides simultaneous optical and UV coverage with the X-ray instruments.

According to the observation requirements, different readout modes can be selected (Lumb et al. 2012), namely full frame, large window, small window, and Timing mode. The MOS and pn cameras provide imaging over the 30′ field of view (FOV) in the energy range of 0.15–15 keV with a spectral resolution of 20–50 ($E/\Delta E$) and angular resolution of 6″.

The Burst Alert Telescope (BAT; Barthelmy et al. 2005) on board the *Swift* mission (Gehrels et al. 2004) observatory is a coded mask aperture instrument with a CdZnTe (CZT) detector with an FOV of 100° × 60°. It operates in the energy range of 15–150 keV with a detection sensitivity of 5.3 mCrab in one day of observation time (Krimm et al. 2013). We used long-term satellite orbitwise light curves to identify the eclipse phases of the eclipsing HMXBs.

We used the catalog of Liu et al. (2000) to select eclipsing HMXBs and then searched for available EPIC pn observations. We shortlisted all EPIC pn observations covering eclipses, comparing with the long-term *Swift*-BAT orbital profiles (Left figures in Figures 1–11). We found eclipse observations of nine HMXBs with a total of 13 observations, 11 of which were

carried out in imaging mode, the other two are in Timing mode. The details of the mode of operation are given in Table 2. We used *XMM-Newton* Science Analysis Software (SAS) version 14.0.0 to reduce the data. We followed Guainazzi et al. (2014) and Kirsch et al. (2006) for the data reduction and region selection for the observations in Timing mode. We followed SAS threads[3,4,5] for the extraction of the light curve and spectra from the cleaned event of the data. We extracted the event files with the SAS tool EVSELECT. We checked for flaring particle background and did not find it in any of the observations. We extracted the events in the energy range of 0.3–12 keV. We first extracted the light curve for the whole duration of each observation, then identified the eclipse and out-of-eclipse (whenever available) durations, comparing it with the long-term average BAT orbital profile and extracted the eclipse and out-of-eclipse events. From these events, we extracted the source along with the background images for each observation. Seeing the image quality, we decided on the size of the source

---

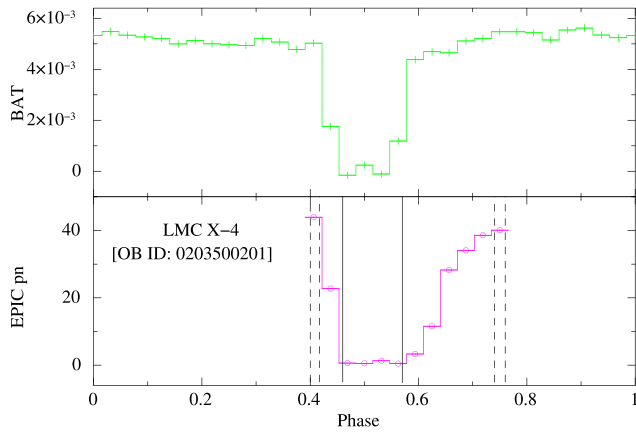3 https://www.cosmos.esa.int/web/xmm-newton/sas-thread-timing
4 https://www.cosmos.esa.int/web/xmm-newton/sas-thread-pn-spectrum
5 https://www.cosmos.esa.int/web/xmm-newton/sas-thread-pn-spectrum-timing

Figure 3. Same as Figure 1 for LMC X-4 (OBS ID: 0203500201).
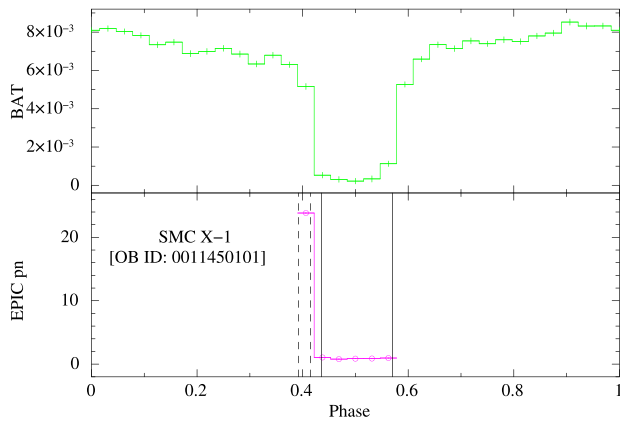

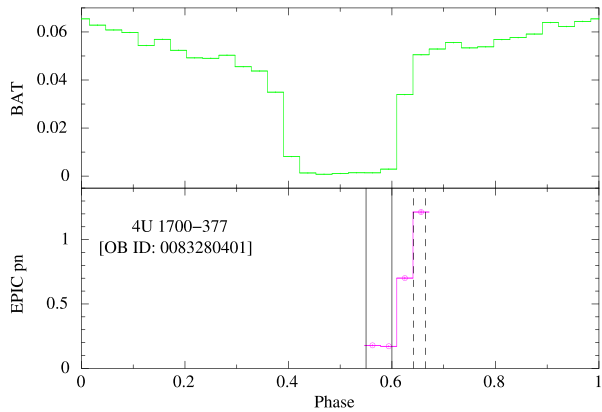**Figure 4.** Same as Figure 1 for SMC X-1 (OBS ID: 0011450101).

Figure 5. Same as Figure 1 for 4U 1700−377 (OBS ID: 0083280401).

region to avoid contribution from excess background counts and the edge of a CCD. In the case of observations in the imaging mode, we extracted $18''$–$30''$ circular source regions. For each observation, we extracted a circular background region of the same size as the source region from a region that is free from any other X-ray sources. In case of the Timing mode, we extracted box regions with $33 \leqslant \mathrm{RAWX} \leqslant 42$ for the source and $3 \leqslant \mathrm{RAWX} \leqslant 5$ for the background for one observation (ID 0203500201) of LMC X-4, with $28 \leqslant \mathrm{RAWX} \leqslant 42$ for the source and $4 \leqslant \mathrm{RAWX} \leqslant 6$ for the background for one

observation (ID 0083280401) of 4U 1700−377. The Timing mode observation of 4U 1700−377 was carried out in the FastBurst submode. For this observation, we extracted the regions with $\mathrm{RAWY} \leqslant 140$ (Kirsch et al. 2006).

Many times, the data are affected by pileup. Pileup causes the energy of two photons detected within one CCD exposure to be added, thus it reduces the number of soft X-ray photons and increases the number of hard X-ray photons, leading to an artificial hardening of the spectrum. Hence, correcting for the pileup is essential. For EPIC pn observations in FullWindow,
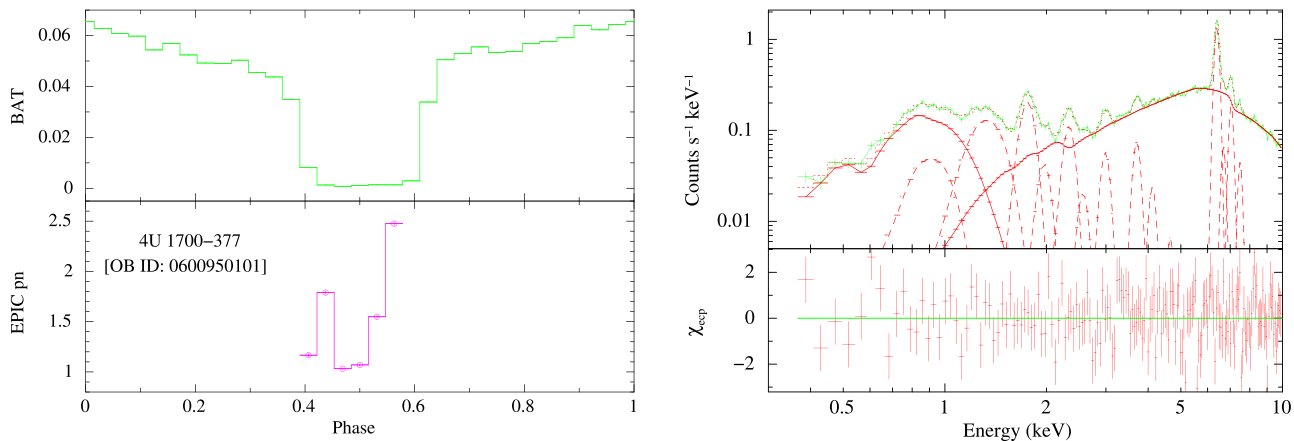
Figure 6. Left figure: the top panel shows the long-term average BAT orbital profile of 4U 1700−377, and the bottom panel shows EPIC pn light curve of 4U 1700−377 (OBS ID: 0600950101) folded with its orbital period. Right figure: the top panel gives the EPIC pn eclipse spectrum of 4U 1700−377 (OBS ID: 0600950101). The bottom panel show the residuals to the best-fit spectral model for the eclipse spectrum.
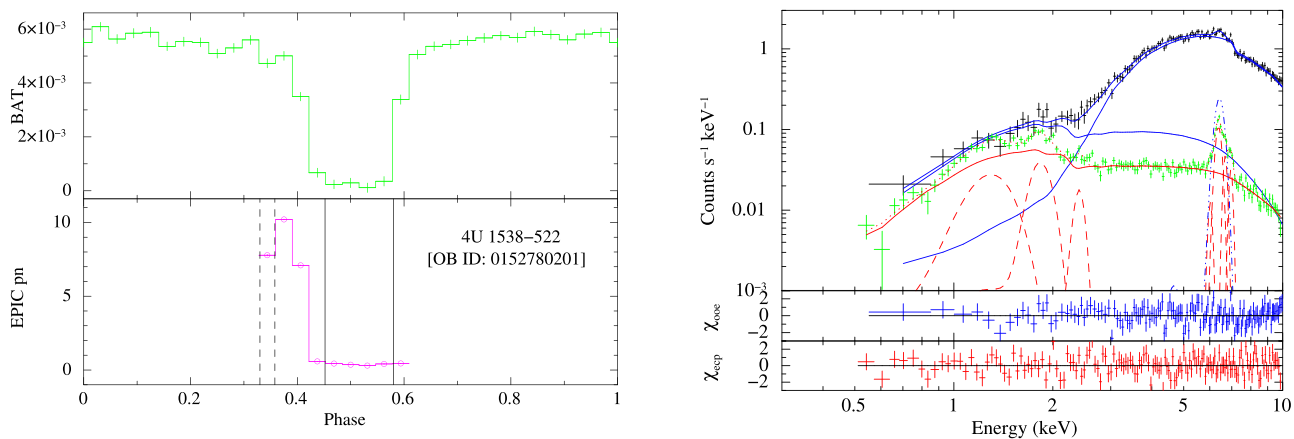

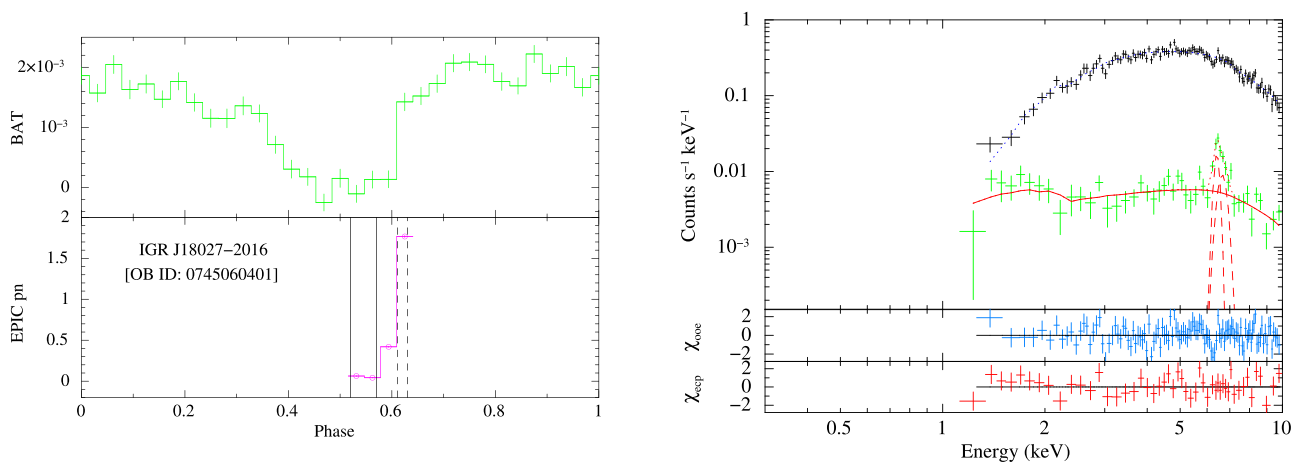**Figure 7.** Same as Figure 1 for 4U 1538−522 (OBS ID: 0152780201).

Figure 8. Same as Figure 1 for IGR J18027−2016 (OBS ID: 0745060401).

LargeWindow, SmallWindow modes, the maximum count rate above which pileup becomes important is 2(4), 3(6), 25(50) for 2.5(5)% flux loss (Jethwa 2012), respectively. However, to check the effect of pileup use of the SAS task, EPATPLOT is recommended.[6] We did not notice pileup in the eclipse data, as the count rate was quite low, compared to the out-of-eclipse

phases. For some of the observations during the out-of-eclipse phases, we noticed a pileup (Cen X-3, OBS ID: 0111010101; LMC X-4, OBS ID: 0142800101; SMC X-1, OBS ID: 0011450101) with the application of the task EPATPLOT. The central part is most likely to be affected by pileup for pointed observations. For the observations affected by pileup, we first removed the part of the point-spread function affected by the pileup, by removing pixels of the central 5″ region and

---
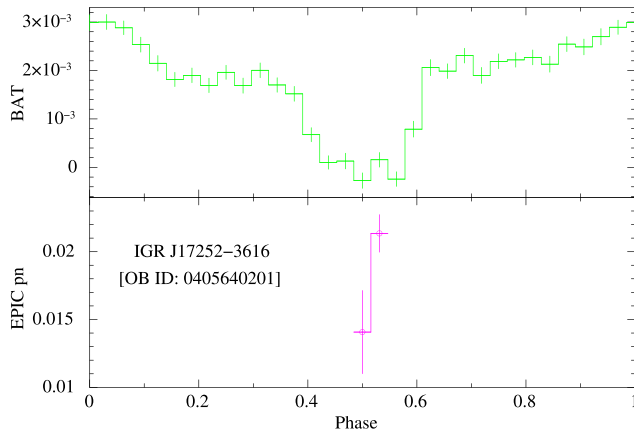
[6] https://www.cosmos.esa.int/web/xmm-newton/sas-thread-epatplot

Figure 9. Same as Figure 6 for IGR J17252−3616 (OBS ID: 0405640201).

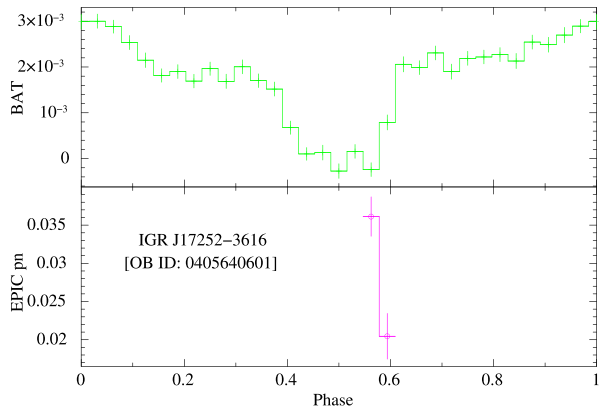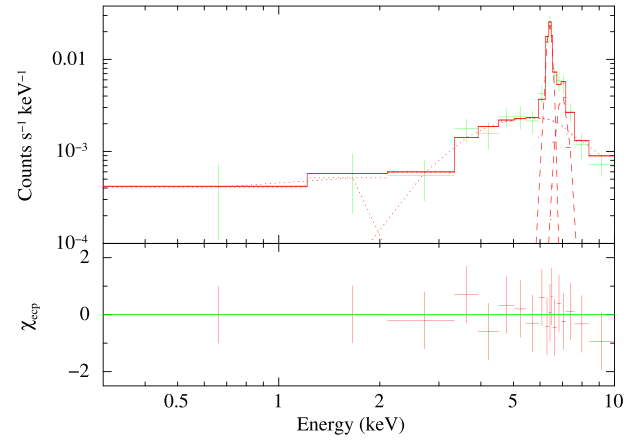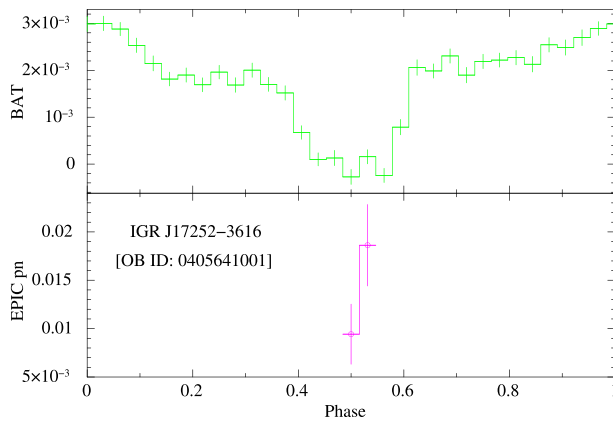**Figure 10.** Same as Figure 6 for IGR J17252−3616 (OBS ID: 0405640601).
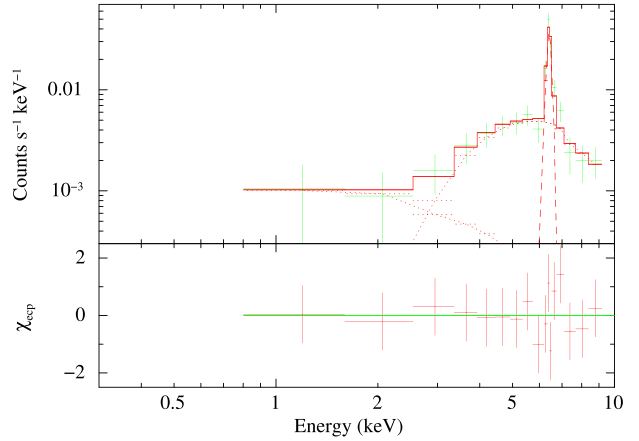
Figure 11. Same as Figure 6 for IGR J17252−3616 (OBS ID: 0405641001).
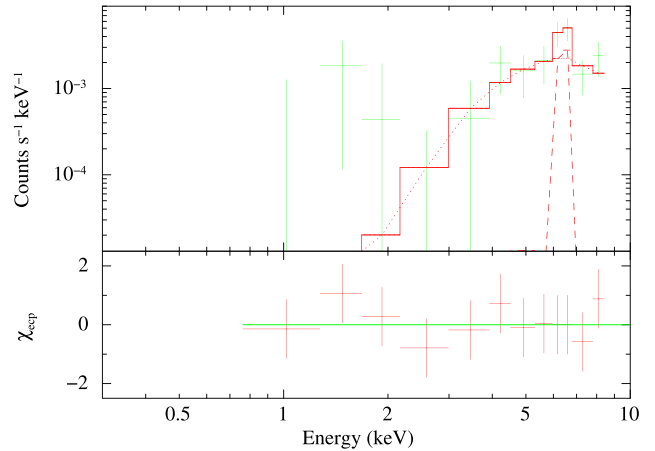
obtaining the spectra. We then extracted spectra from an annular source region of inner radius 10″. We found stable spectral parameters for the same best-fit model in both cases, then finally, we obtained the spectra with annular source regions of 5″ inner radius for the observations in which we noticed pileup.

2.1. Event Selection from the Light Curves

We extracted source and background light curves from the source and background region file from the single and double events (with PATTERN ⩽ 4), respectively, for the full exposure time for each observation with the SAS task EVSELECT. We subtracted the background light curve from the source light curve to obtain the background-subtracted source light curve using the FTOOL LCMATH. We confirmed the eclipse and the out-of-eclipse phases (whenever available) by plotting the EPIC pn light curve along with the average orbital profile of the long-term *Swift*-BAT light curve (Krimm et al. 2013) for each observation. In the left panels of Figures 1–13, the top panels show the long-term *Swift*-BAT

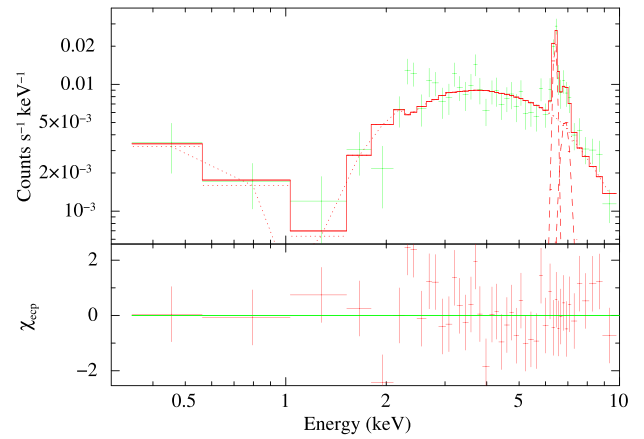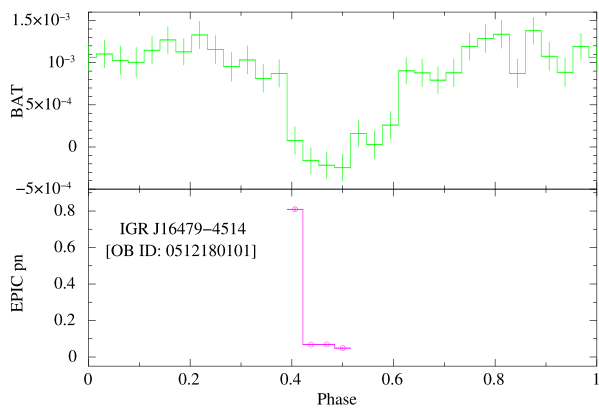**Figure 12.** Same as Figure 6 for IGR J16479−4514 (OBS ID: 0512180101).

Table 2
The *XMM-Newton* EPIC pn Log of Observations of the HMXBs

Source	Observation ID	Date of Observation	Datamode	Submode	Effective Exposure (s)	Average Count-rate (c s^{-1}) (OOE)
Cen X-3	0111010101	2001 Jan 27	IMAGING	PrimeSmallWindow	67250	41.37
LMC X-4	0142800101	2003 Sep 9	IMAGING	PrimeSmallWindow	113171	51.05
LMC X-4	0203500201	2004 Jun 16	TIMING	FastTiming	41360	43.21
SMC X-1	0011450101	2001 May 31	IMAGING	PrimeFullWindow	56389	54.57
4U 1700−377	0083280401	2001 Feb 20	TIMING	FastBurst	30448	22.05
4U 1700−377	0600950101	2009 Sep 1	IMAGING	PrimeFullWindow	49533	...
4U 1538−522	0152780201	2003 Aug 14	IMAGING	PrimeFullWindow	79035	10.33
IGR J18027−2016	0745060401	2014 Sep 11	IMAGING	PrimeFullWindow	43041	2.89
IGR J17252−3616	0405640201	2006 Aug 29	IMAGING	PrimeLargeWindow	20672	...
IGR J17252−3616	0405640601	2006 Sep 8	IMAGING	PrimeFullWindow	12104	...
IGR J17252−3616	0405641001	2006 Sep 27	IMAGING	PrimeLargeWindow	10172	...
IGR J16479−4514	0512180101	2008 Mar 21	IMAGING	PrimeSmallWindow	32752	...
IGR J16418−4532	0679810101	2012 Sep 1	IMAGING	PrimeLargeWindow	18281	...

Note. OOE: out-of-eclipse.

orbital profiles and the bottom panels the EPIC pn light curves. We mark the duration of eclipse events within two solid lines and that of the out-of-eclipse persistent phases within two dashed lines.

Then, we extracted separately the (1) eclipse events and the (2) out-of-eclipse persistent events from the event files, for the observations that cover both the eclipse and out-of-eclipse phases. For the observations that were taken during eclipse phases only, we extracted the eclipse events from the full event files of those observations. To generate the eclipse and out-of-eclipse event files, we first noticed the start and end times of each phase, then used the SAS task GTIBUILD to generate good time intervals of the two phases. Then, using the SAS task EVSELECT, we extracted the eclipse and out-of-eclipse events (whenever available) for each observation.

2.2. Spectral Analysis

We extracted the spectra for both the eclipse and out-of-eclipse phases (when available) from the single and double events (with PATTERN ⩽ 4), excluding the events that are at the edge of a CCD and at the edge of a bad pixel (with FLAG = 0). To extract the spectra, we used the SAS task EVSELECT. We generated response and ancillary files using the SAS tasks RMFGEN and ARFGEN, respectively. We then extracted spectra from these eclipse events for each observation and from the events during out-of-eclipse persistent phases whenever available. We rebinned the spectra with 25 counts per bin with the SAS routine SPECGROUP and therefore used χ^2 statistics. Observations with IDs 0405640201, 0405640601, and 0405641001 of IGR J17252−3616; 0679810101 of IGR J16418−4532; 0600950101 of 4U 1700−377 were taken only during eclipse; observation 0512180101 of IGR J16479−4514 covers a small part of the ingress along with the total eclipse phase. So, for these six observations, no out-of-eclipse spectra are available. We fitted the X-ray spectra using XSPEC v12.8.2.

The out-of-eclipse spectra and the eclipse spectra are shown in the top panels of each figure on the right in Figures 1–5 and in Figures 7 and 8), where the middle and bottom panels show the contribution of each bin toward the χ for the out-of-eclipse and eclipse spectra, respectively. The top-right panel of Figures 6 and 9–13 show the eclipse spectra of these six observations, where the bottom panels show the contribution of χ for each bin for the eclipse spectra only.
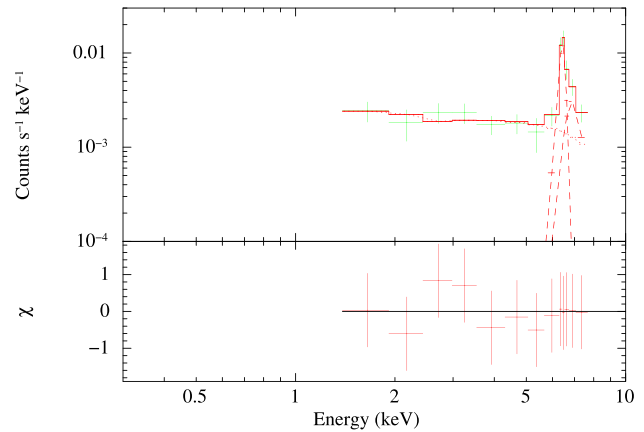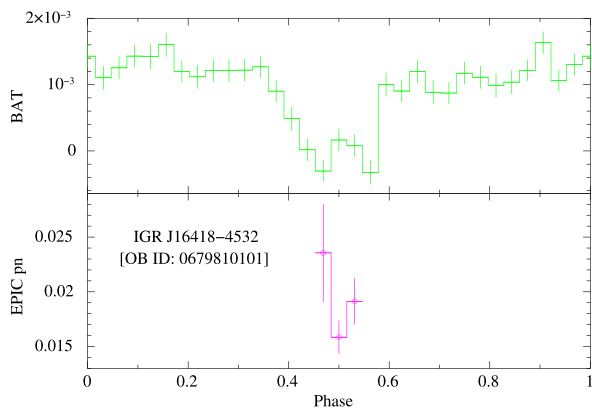
Figure 13. Same as Figure 6 for IGR J16418−4532 (OBS ID: 0679810101).

2.2.1. Eclipse and Out-of-eclipse Spectra of the HMXBs

The eclipse spectra were primarily fitted with the XSPEC model powerlaw modified by photoelectric absorption with model phabs to account for the Galactic line of sight and local absorption, and a high-energy cutoff (XSPEC model highecut) for some sources. A few of the sources showed excess low-energy emission. and a blackbody component (XSPEC model bbodyrad) was added to the model for these sources. Excess narrow emission profiles were seen in some of the spectra at specific energies. The excess at specific energies was fitted with Gaussian functions (XSPEC model Gauss). Some sources show a significant soft excess below 1.5 keV while the power-law component is highly absorbed. The soft excess, therefore, cannot originate at the same location as the power law for these observations. We fitted the soft excess as a blackbody (XSPEC model bbodyrad) with a different absorption column density from those observations (model phabs), only for the purpose of characterizing its temperature and flux. If the soft excess originates in a much larger region elsewhere in the binary, its true nature may not be a blackbody, and a bremsstrahlung may be a more appropriate description. So for spectra in which the soft excess could not be fitted with a blackbody, XSPEC model bremss was used. We note that several eclipse spectra showed a very low even a slightly negative photon index in the 1–10 keV band. However, this does not lead to a large bolometric luminosity as the accretion-powered pulsars have an exponential cutoff, which is usually above 10 keV and outside the EPIC pn energy band. The details of the models can be found online in the HEASARC webpage.[7] The best-fit parameters for the eclipse and out-of-eclipse spectra for all eclipsing HMXBs and details of the individual sources are discussed below.

Cen X-3: Ebisawa et al. (1996) carried out spectral analysis of *ASCA* data in the pre-eclipse, ingress, eclipse, and egress phases in two energy bands (0.7–4 and 5–10 keV). In the high-energy band, they obtained best fits with a cutoff power law modified by photoelectric absorption along the line of sight, an Fe edge (∼7.1–7.2 keV), and four Gaussian functions for Fe K_α (∼6.4, ∼6.7, and ∼6.97 keV), and Fe K_β (fixed with 7.06 keV) emission lines. In the low-energy band, they fitted the above spectra with an absorbed power law with four to six emission lines. The broadband (0.5–70 keV) eclipse and out-of-eclipse spectra of Cen X-3 with *Suzaku* (Naik et al. 2011) were well fitted with a partial coverage power-law model with a

high-energy cutoff and Gaussian functions for the three Fe emission lines (6.4, 6.7, and 6.97 keV). Naik & Paul (2012) obtained the best fit with *XMM-Newton* eclipse and out-of-eclipse spectra in the energy range of (4–10 keV) with a power law and three Gaussian functions for the above three Fe emission lines. Power-law photon indices were found to be lowest in the eclipse phase, which then increases with the increase of flux.

The EPIC pn observation of Cen X-3 (OBS ID: 0111010101) covers a large fraction of the total eclipse, eclipse egress, and a small part of the out-of-eclipse persistent phase. The eclipse spectrum of this observation was best fitted with a power law, a blackbody emission (bbodyrad), and eight Gaussian functions for emission lines at 0.98, 1.43, 1.98, 2.62, 3.34, 6.41, 6.66, and 6.94 keV modified by photoelectric absorption. The out-of-eclipse spectrum has been fitted with the same model used for the best fit of the eclipse spectrum but with different model parameters. The details are given in Tables 3–5. In the out-of-eclipse phase, the power-law photon index is slightly smaller, and the total flux in the energy range of (0.3–10) keV is larger by a factor of ∼10 compared to the eclipse phase. We detected three Fe emission lines (fluorescent Fe K_α, Fe XXV, and Fe XXVI) in both the eclipse and the out-of-eclipse phases. The fluxes for the three lines are 0.88, 2.12, and 1.65, respectively, in the eclipse phase and 15.01, 11.64, and 9.58, respectively, in the out-of-eclipse phase, in units of 10^{-4} photons cm^{-2} s^{-1}. The corresponding equivalent widths are ∼104^{+9}_{-11} eV, ∼246^{+10}_{-12} eV, and ∼209^{+11}_{-11} eV in the eclipse phase, and ∼189^{+12}_{-8} eV, ∼131^{+5}_{-7} eV, and 139^{+7}_{-7} eV in the out-of-eclipse phase respectively. The Fe K_α emission line flux increases more than 17 times, and the corresponding equivalent width increases by a factor of ∼2 in the out-of-eclipse phase compared to the eclipse phase. An increase of the equivalent width in the out-of-eclipse phase from the eclipse phase is not expected when the emitting material is distributed in an extended region. The fluxes of the Fe XXV and Fe XXVI emission lines increase by a factor of more than 5, but their equivalent widths fall by a factor of ∼2 in the out-of-eclipse phase compared to their values in the eclipse phase. An increase in the equivalent width of fluorescent Fe K_α emission lines has been observed in the out-of-eclipse phase compared to the eclipse phase earlier from the same *XMM-Newton* observation (Naik & Paul 2012) and from an *ASCA* observation of Cen X-3 (Ebisawa et al. 1996).

Table 3
The Exposure Times for the Eclipse and the Out-of-eclipse Spectra of the HMXBs and the Best-fit Spectral Models

Source	Observation ID	Phase	Exposure	Best-fit Model
Cen X-3	0111010101	E	7152	$phabs_1 \times (bbodyrad_2 + gaussian_3 + gaussian_4 + gaussian_5 + gaussian_6 + gaussian_7 + gaussian_8 + gaussian_9 + gaussian_{10} + powerlaw_{11})$
Cen X-3	0111010101	OOE	8937	$phabs_1 \times (gaussian_2 + gaussian_3 + bbodyrad_4 + gaussian_5 + gaussian_6 + gaussian_7 + gaussian_8 + gaussian_9 + gaussian_{10} + powerlaw_{11})$
LMC X-4	0142800101	E	8972	$phabs_1 \times (powerlaw_2 + bbodyrad_3 + gaussian_4)$
LMC X-4	0142800101	OOE	38170	$phabs_1 \times (powerlaw_2 + bremss_3 + bbodyrad_4 + gaussian_5 + gaussian_6)$
LMC X-4	0203500201	E	11630	$phabs_1 \times (bbodyrad_2 + powerlaw_3)$
LMC X-4	0203500201	OOE	6336	$phabs_1 \times (bremss_2 + gaussian_3 + gaussian_4 + gaussian_5 + powerlaw_6)$
SMC X-1	0011450101	E	30790	$phabs_1 \times (highecut_2 \times powerlaw_3 + bbodyrad_4 + gaussian_5)$
SMC X-1	0011450101	OOE	808	$phabs_1 \times (highecut_2 \times powerlaw_3 + bbodyrad_4)$
4U 1700−377	0083280401	E	622	$phabs_1 \times (powerlaw_2 + gaussian_3)$
4U 1700−377	0083280401	OOE	34	$phabs_1 \times (powerlaw_2 + gaussian_3)$
4U 1700−377	0600950101	E	42790	$edge_1 \times phabs_2 \times (bbodyrad_3 + gaussian_4 + gaussian_5 + gaussian_6 + gaussian_7 + gaussian_8 + gaussian_9 + gaussian_{10} + gaussian_{11} + gaussian_{12} + gaussian_{13} + gaussian_{14} + gaussian_{15} + gaussian_{16} + highecut_{17} \times powerlaw_{18})$
4U 1538−522	0152780201	E	44780	$phabs_1 \times (powerlaw_2 + gaussian_3 + gaussian_4 + gaussian_5 + gaussian_6 + gaussian_7 + gaussian_8 + gaussian_9)$
4U 1538−522	0152780201	OOE	3171	$phabs_1 \times (gaussian_2 + powerlaw_3) + phabs_4 \times bbodyrad_5$
IGR J18027−2016	0745060401	E	22150	$phabs_1 \times (powerlaw_2 + gaussian_3 + gaussian_4)$
IGR J18027−2016	0745060401	OOE	4347	$phabs_1 \times powerlaw_2$
IGR J17252−3616	0405640201	E	19190	$phabs_1 \times (powerlaw_2 + gaussian_3 + gaussian_4) + phabs_5 \times bbodyrad_6$
IGR J17252−3616	0405640601	E	10620	$phabs_1 \times (powerlaw_2 + gaussian_3) + phabs_4 \times bbodyrad_5$
IGR J17252−3616	0405641001	E	9431	$phabs_1 \times (powerlaw_2 + gaussian_3)$
IGR J16479−4514	0512180101	E	18730	$phabs_1 \times (gaussian_2 + gaussian_3 + powerlaw_4) + phabs_5 \times bbodyrad_6$
IGR J16418−4532	0679810101	E	16990	$phabs_1 \times (powerlaw_2 + gaussian_3 + gaussian_4)$

LMC X-4: Naik & Paul (2004b) reported three different fits of the *BeppoSAX* spectra in the low state of LMC X-4, among which the fit with a power law, a bremsstrahlung component ($kT \sim 0.4$ keV), and a Gaussian function for the 6.4 keV Fe emission line, together modified by the line-of-sight photo-electric absorption, is reported to be the best. The best fit for the high state of *BeppoSAX* spectra was obtained with two absorbed power laws (hard with $\Gamma \sim 0.65$, soft with $\Gamma \sim 3$),

a blackbody component ($kT \sim 0.15$ keV), and a Gaussian function for the 6.4 keV Fe emission line. Neilsen et al. (2009) obtained the *XMM-Newton*-RGS and *Chandra* High-Energy Transmission Grating Spectrometer (HETGS) spectra in the hard and low states of LMC X-4, respectively. They obtained the best fit of the RGS spectra with power-law, bremsstrahlung ($kT \sim 0.455$ keV), and blackbody ($kT \sim 0.043$ keV) components and Gaussian functions for many emission lines of

nitrogen and oxygen, all modified by line-of-sight photoelectric absorption. HETGS spectra gave the best fit with a model comprising power-law, bremsstrahlung ($kT \sim 0.43$ keV), and Gaussian functions corresponding to different species of emission lines of neon, nitrogen, and oxygen, and three Fe K_α emission lines, modified with photoelectric absorption.

We analyzed two EPIC pn observations of LMC X-4, where the first one was on 2003 September 9 and the second one was on 2004 June 16th. The first EPIC pn observation of LMC X-4 (OBS ID: 0142800101) covers three pre-eclipse bursts, the out-of-eclipse persistent emission, eclipse ingress, full length of the total eclipse, and eclipse egress. The other observation of this source (OBS ID: 0203500201) included the out-of-eclipse persistent phase, eclipse ingress, and full length of the total eclipse, including a small burst and the eclipse egress phase. In the first EPIC pn observation (OBS ID: 0142800101) of LMC X-4, there were three bursts at the beginning of the observation. For the out-of-eclipse spectrum for this observation, we excluded the period of the bursts and only used data where the source intensity was steady, as shown by the dashed lines in the left panel of Figure 2. The pulse profile evolution of LMC X-4 during and after the flares was reported from this observation by Beri & Paul (2017). In the other observation (OBS ID: 0203500201) of LMC X-4, where a small burst was found during the eclipse, we extracted the eclipse spectrum for this observation excluding the events during the bursts. The eclipse spectrum of the first observation (OBS ID: 0142800101) of LMC X-4 is fitted with a power law, a blackbody, and a Gaussian function for the Fe K_α emission line modified by line-of-sight photoelectric absorption. The X-ray spectrum of LMC X-4 shows very low absorption column density (N_H). N_H could not be constrained with the *XMM-Newton* spectrum. The X-ray spectrum of LMC X-4 was detected down to 0.1 keV with the LECS instrument of *BeppoSAX* (Naik & Paul 2004b) with very low N_H. We took the Galactic column density of 0.06×10^{22} cm^{-2} toward LMC X-4 (HEASARC TOOL[8]) as the lower limit of the absorption column density for the X-ray spectrum. The power-law photon index was obtained to be $0.0^{+0.3}_{-0.3}$ for the eclipse spectrum. The best-fit value for the energy of the fluorescent Fe K_α emission line is 6.36 keV with a flux of 0.07×10^{-4} photons cm^{-2} s^{-1}. For the out-of-eclipse spectrum of this observation, the best spectral fit is obtained with a model consisting of a power law, blackbody emission, bremsstrahlung radiation, and two Gaussian functions (one for the Fe XXV emission line, another for a low-energy emission line), modified by photoelectric absorption. N_H is frozen at the same value as for the eclipse spectrum. Beri & Paul (2017) obtained similar parameters with this model, in the best fit of the phase-averaged persistent spectrum of the same EPIC pn observation. In the out-of-eclipse phase, the power-law photon index increases by $\sim$0.7, and the total flux in the energy range of (0.3–10) keV is larger by a factor of more than 237 compared to the eclipse phase. The low-ionization (or neutral) Fe K_α emission line was detected during eclipse with high equivalent width (597^{+171}_{-256} eV), but it is absent in the out-of-eclipse phase (upper limit of equivalent width $\sim$20 eV), while a highly ionized 6.60 keV Fe XXV emission line was detected in the out-of-eclipse phase, with line flux of 4.03×10^{-4} photons cm^{-2} s^{-1} and equivalent width of $\sim$166$^{+12}_{-11}$ eV, but it is absent in the

eclipse phase. We obtained a low-energy emission line with energy $0.96^{+0.01}_{-0.01}$ keV. Neilsen et al. (2009) detected the 13.560 Å (0.91 keV) Ne IX He$_\alpha$ and 12.158 Å (1.02 keV) Ne X Ly$_\alpha$ emission lines near 1 keV with the *Chandra* HETGS. The 0.96 keV line detected by EPIC pn could be a mix of the two lines at 0.91 and 1.02 keV of Ne, seen earlier with the HETGS instrument.

The second observation of LMC X-4 (OBS ID: 0203500201) was carried out in Timing mode. The best-fit model for the eclipse spectrum of this observation is obtained with a power law and a blackbody emission modified by photoelectric absorption. The line-of-sight hydrogen column density is fixed to 0.06×10^{22} cm^{-2} for the eclipse spectrum, similar to the eclipse and out-of-eclipse spectra of the previous observation of this source. The out-of-eclipse spectrum of this observation was best fitted with a power law, a bremsstrahlung radiation, and three Gaussian functions of emission energies 0.98, 6.38, and 6.99 keV, modified by photoelectric absorption with N_H frozen with a value of 0.06×10^{22} cm^{-2}. The power-law photon index in the out-of-eclipse phase increases by $\sim$0.8, while the total flux in the energy range of (0.3–10) keV is larger by a factor of 86 compared to the eclipse phase. We detected fluorescent Fe K_α emission line in the out-of-eclipse phase with a flux of 1.55×10^{-4} photons cm^{-2} s^{-1} and the equivalent width of $\sim$117$^{+2}_{-2}$ eV. The Fe XXVI emission line was detected in the out-of-eclipse phase with a flux of 2.39×10^{-4} photons cm^{-2} s^{-1} and an equivalent width of $\sim$195$^{+4}_{-3}$ eV, respectively. In the eclipse spectrum, we found some positive residuals in the (6–7) keV energy range, but due to poor statistics, we could not constrain the energy of the emission lines. However, just to compare the line fluxes, we fitted the eclipse spectrum with the two Fe emission lines (fluorescent Fe K_α and Fe XXVI), freezing the line energy and width as obtained in the out-of-eclipse spectrum. Including these lines, we obtained very little improvement in the χ^2, from a value of 103.01 for 94 degrees of freedom to 99.93 with 92 degrees of freedom. We found the flux of 2.59×10^{-6} photons cm^{-2} s^{-1} for the fluorescent Fe K_α emission line and 2.80×10^{-6} photons cm^{-2} s^{-1} for the Fe XXVI emission line, which are less significant than 3σ. Like the out-of-eclipse phase of the previous observation, the $0.98^{+0.03}_{-0.03}$ keV emission line could be a sum of the two Ne lines detected by Neilsen et al. (2009) with *Chandra* HETGS.

SMC X-1: Naik & Paul (2004a fitted the pulse-phase-average spectra with *BeppoSAX* by a hard power-law component with a high-energy cutoff, a blackbody emission for the soft excess, and a Gaussian function for the 6.4 keV Fe emission line modified by photoelectric absorption. Hu et al. (2013) analyzed both the hard- and soft-state spectra of SMC X-1 with *RXTE*-PCA. They best describe the continuum of both spectra with a Comptonized component, a blackbody emission, and a Gaussian function for the 6.4 keV Fe emission line. They found lower plasma temperature, Fe line width, and equivalent width in the low state compared to those in the hard state.

The EPIC pn observation of SMC X-1 (Observation ID: 0011450101) covers a very small portion of the out-of-eclipse persistent phase, eclipse ingress and full length of the total eclipse. The eclipse spectrum of SMC X-1 has been modeled with a power law with a high-energy cutoff, a blackbody emission, and a Gaussian function for the Fe K_α emission line of 6.38 keV modified by photoelectric absorption. The high-energy cutoff was found to have a value of 2.46 keV with a

---

Table 4
Line-of-sight Hydrogen Column Density (N_H), Photon Index (Γ), Blackbody Temperature (T_{BB}), χ^2/DOF, and Total Flux in the Energy Range of (0.3–10.0) keV for Nine Eclipsing HMXB Systems during the Eclipse (E) and Out-of-eclipse (OOE) Phases

Source	Observation ID	Phase	N_H $(10^{22}$ $cm^{-2})$	Photon Index (Γ)	T_{BB} (keV)	χ^2 (DOF)	Total Flux $(10^{-11}$ erg cm^{-2} $s^{-1})$
Cen X-3	0111010101	E	$1.50^{+0.10}_{-0.11}$	$0.71^{+0.02}_{-0.06}$	$0.14^{+0.01}_{-0.01}$	197.73 (127)	4.47
Cen X-3	0111010101	OOE	$2.07^{+0.18}_{-0.16}$	$0.51^{+0.05}_{-0.02}$	$0.08^{+0.01}_{-0.01}$	207.39 (137)	43.74
LMC X-4	0142800101	E	0.06 (frozen)	$0.0^{+0.3}_{-0.3}$	$0.22^{+0.03}_{-0.03}$	38.83 (37)	0.11
LMC X-4	0142800101	OOE	0.06 (frozen)	$0.74^{+0.01}_{-0.01}$	$0.044^{+0.005}_{-0.005}$	1129.22 (718)	26.09
LMC X-4	0203500201	E	0.06 (frozen)	$0.08^{+0.20}_{-0.21}$	$0.18^{+0.02}_{-0.01}$	103.01 (94)	0.18
LMC X-4	0203500201	OOE	0.06 (frozen)	$0.88^{+0.04}_{-0.04}$	$\cdots$	151.81 (145)	15.48
SMC X-1	0011450101	E	$0.03^{+0.02}_{-0.02}$	$-0.56^{+0.23}_{-0.25}$	$0.23^{+0.02}_{-0.01}$	181.73 (147)	0.52
SMC X-1	0011450101	OOE	$0.06^{+0.03}_{-0.03}$	$0.20^{+0.17}_{-0.17}$	$0.21^{+0.02}_{-0.02}$	198.21 (156)	39.84
4U 1700−377	0083280401	E	$0.62^{+1.10}_{-0.62}$	$-0.41^{+0.26}_{-0.24}$	$\cdots$	88.60 (71)	4.28
4U 1700−377	0083280401	OOE	$23.17^{+19.36}_{-6.36}$	$-0.17^{+0.52}_{-0.55}$	$\cdots$	23.96 (18)	34.28
4U 1700−377	0600950101	E	$1.01^{+0.32}_{-0.43}$	$-1.34^{+0.14}_{-0.14}$	$0.08^{+0.04}_{-0.06}$	195.06 (133)	3.19
4U 1538−522	0152780201	E	$0.36^{+0.08}_{-0.05}$	$0.22^{+0.06}_{-0.06}$	$\cdots$	178.19 (130)	0.46
4U 1538−522	0152780201	OOE	$17.16^{+1.17}_{-1.12}$	$0.71^{+0.08}_{-0.08}$	$1.53^{+0.88}_{-0.42}$	125.90 (126)	13.93
IGR J18027−2016	0745060401	E	$0.36^{+0.53}_{-0.36}$	$-0.22^{+0.24}_{-0.23}$	$\cdots$	49.28 (41)	0.08
IGR J18027−2016	0745060401	OOE	$5.90^{+0.40}_{-0.37}$	$0.71^{+0.08}_{-0.08}$	$\cdots$	110.04 (110)	3.47
IGR J17252−3616	0405640201	E	$9.34^{+137.59}_{-6.46}$	$0.24^{+0.83}_{-0.75}$	$0.19^{+4.92}_{-0.10}$	6.23 (7)	0.04
IGR J17252−3616	0405640601	E	$18.17^{+24.96}_{-12.15}$	$0.81^{+4.92}_{-1.17}$	$1.07^{+0.01}_{-0.001}$	7.66 (8)	0.05
IGR J17252−3616	0405641001	E	$13.48^{+43.32}_{-13.48}$	$-0.52^{+4.35}_{-2.47}$	$\cdots$	3.50 (6)	0.03
IGR J16479−4514	0512180101	E	0.58 (frozen)	$1.28^{+0.37}_{-0.34}$	$0.07^{+0.39}_{-0.09}$	44.67 (36)	0.08
IGR J16418−4532	0679810101	E	$0.84^{+1.43}_{-0.84}$	$0.40^{+0.83}_{-0.45}$	$\cdots$	2.13 (5)	0.03

folding energy of 3.6 keV. The best fit for the out-of-eclipse spectrum is found with the above model except the Fe K$_\alpha$ emission line. The high-energy cutoff is found to have a value of 2.59 keV with a folding energy of 8.12 keV. The power-law photon index has a negative value ($\Gamma = -0.56$) in the eclipse phase, and it increases to 0.2 in the out-of-eclipse phase. We also obtain a good fit for the eclipse spectrum with the same model as mentioned above for this phase with the same power-law photon index (0.2) as obtained for the best fit of the out-of-eclipse spectrum, but with the parameters for the high-energy cutoff and folding energy nearly doubling their values. The χ^2 (194.10) for this fit is higher than the χ^2 (181.73) of the previous fit. So we report the parameter values in Tables 4 and 5 from the previous fit only. The total flux in the energy range of (0.3–10) keV in the out-of-eclipse phase is larger by a factor of ~77 compared to its value in the eclipse phase. During the eclipse phase, we detected a fluorescent Fe K$_\alpha$ emission line with flux and equivalent width of 0.07×10^{-4} photons cm^{-2} s^{-1} and 126^{+18}_{-18} eV, respectively. We could not detect any Fe K$_\alpha$ emission line during the out-of-eclipse phase, but we cannot rule out this line as the duration of the out-of-eclipse phase compared to the eclipse phase is very short (lower by a factor of ~44) and the continuum flux is higher by a large factor (~77 times) in the out-of-eclipse phase than the eclipse phase. We derived an upper limit of the equivalent width of ~90 eV for an emission line of 6.4 keV in the out-of-eclipse phase.

4U 1700−377: van der Meer et al. (2005) obtained three different fits for the continuum of the eclipse, eclipse egress, and low-flux spectra of 4U 1700−377 with *XMM-Newton*. The first model comprises three power-law components, one for the direct X-rays from the compact object, another for the scattered X-rays from the surrounding medium, and the third is for the soft excess. While the second model is described with the first

two power laws modified with a high-energy cutoff, and in the third model, the power law for the soft excess was replaced with a blackbody component. Several Gaussian functions were included for the emission lines in all spectra. The three fits gave similar reduced χ^2. Among the possible Fe emission lines, the 6.4 keV and 6.53 keV Fe K$_\alpha$ and 7.06 keV Fe K$_\beta$ emission lines were found during eclipse, the 6.42, 6.72, and 7.11 keV Fe emission lines were observed in the egress, and the 6.41 keV, 6.72 keV (fixed) and 7.06 keV (fixed) Fe emission lines were detected in the low-flux state. The 6.53 keV Fe emission line seen during eclipse was suggested to come from higher ionized Fe ions (Fe XVIII–XXIV). The relation between the ionization parameters for different lines and line intensities indicate photoionized plasma surrounding the central source. The fit of the soft excess could not give a satisfactory explanation of its origin. Previously with *GINGA*, the soft excess was fitted with a bremsstrahlung component (Haberl & Day 1992; Haberl et al. 1994), the temperature of which could not be constrained.

We analyzed two EPIC pn observations of 4U 1700−377 (OBS IDs: 0083280401, 0600950101) carried out on 2001 February 20–21 for ~30 ks and on 2009 September 1 for ~50 ks. The first one covers some part of the eclipse, the eclipse egress, and a small portion of the out-of-eclipse persistent phase, and the second one covers nearly the full length of the eclipse phase. The first observation (OBS ID: 0083280401) was carried out in Timing FastBurst mode. For the eclipse spectrum in this observation, the best fit was obtained with a power-law and Gaussian function with energy 6.37 keV modified by photoelectric absorption. This observation includes a shorter duration of the eclipse, and the spectrum has limited statistics. The best fit for the out-of-eclipse spectrum of this observation is also obtained with the above

Table 5
Fe K$_\alpha$ (Fluorescent), Fe XXV, and Fe XXVI Emission Line Energy, Flux, and Equivalent Width for Nine HMXBs during Eclipse (E) and Out-of-eclipse (OOE) Phases

Source	Observation ID	State	Fe K$_\alpha$ Line Energy (keV)	Fe K$_\alpha$ Line Flux	Fe K$_\alpha$ Line Eqv. Width (eV)	Fe XXV Line Energy (keV)	Fe XXV Line Flux	Fe XXV Line Eqv. Width (eV)	Fe XXVI Line Energy (keV)	Fe XXVI Line Flux	Fe XXVI Line Eqv. Width (eV)
Cen X-3	0111010101	E	$6.41^{+0.05}_{-0.03}$	$0.88^{+0.08}_{-0.09}$	104^{+9}_{-11}	$6.66^{+0.01}_{-0.01}$	$2.12^{+0.09}_{-0.1}$	246^{+10}_{-12}	$6.94^{+0.01}_{-0.01}$	$1.65^{+0.09}_{-0.09}$	209^{+11}_{-11}
Cen X-3	0111010101	OOE	$6.41^{+0.01}_{-0.01}$	$15.01^{+0.93}_{-0.66}$	189^{+12}_{-8}	$6.68^{+0.01}_{-0.01}$	$11.64^{+0.45}_{-0.58}$	131^{+5}_{-7}	$6.98^{+0.01}_{-0.01}$	$9.58^{+0.49}_{-0.50}$	139^{+7}_{-7}
LMC X-4	0142800101	E	$6.36^{+0.26}_{-0.11}$	$0.07^{+0.02}_{-0.03}$	597^{+171}_{-256}	...	...	...	...	...	...
LMC X-4	0142800101	OOE	...	...	...	$6.60^{+0.04}_{-0.03}$	$4.03^{+0.28}_{-0.26}$	166^{+12}_{-11}	...	...	...
LMC X-4	0203500201	OOE	$6.38^{+0.04}_{-0.04}$	$1.55^{+0.03}_{-0.03}$	117^{+2}_{-2}	...	...	...	$6.99^{+0.05}_{-0.05}$	$2.39^{+0.05}_{-0.04}$	195^{+4}_{-3}
SMC X-1	0011450101	E	$6.38^{+0.06}_{-0.06}$	$0.07^{+0.01}_{-0.01}$	126^{+18}_{-18}	...	...	...	...	...	...
SMC X-1	0011450101	OOE	...	...	...	...	...	...	...	...	...
4U 1700−377	0083280401	E	$6.37^{+0.02}_{-0.02}$	$5.96^{+0.48}_{-0.49}$	1258^{+101}_{-103}	...	...	...	...	...	...
4U 1700−377	0083280401	OOE	$6.44^{+0.06}_{-0.06}$	$14.88^{+5.55}_{-5.43}$	191^{+71}_{-70}	...	...	...	...	...	...
4U 1700−377	0600950101	E	$6.39^{+0.002}_{-0.002}$	$4.89^{+0.06}_{-0.06}$	1061^{+13}_{-13}	$6.68^{+0.05}_{-0.04}$	$0.26^{+0.05}_{-0.04}$	22^{+4}_{-3}	...	...	...
4U 1538−522	0152780201	E	$6.38^{+0.01}_{-0.01}$	$0.57^{+0.03}_{-0.03}$	792^{+42}_{-42}	$6.69^{+0.02}_{-0.02}$	$0.17^{+0.02}_{-0.02}$	145^{+17}_{-17}	$6.95^{+0.02}_{-0.02}$	$0.13^{+0.01}_{-0.01}$	181^{+14}_{-14}
4U 1538−522	0152780201	OOE	$6.42^{+0.07}_{-0.07}$	$2.46^{+0.64}_{-0.57}$	79^{+22}_{-18}	...	...	...	...	...	...
IGR J18027−2016	0745060401	E	$6.41^{+0.06}_{-0.05}$	$0.07^{+0.04}_{-0.03}$	445^{+254}_{-191}	$6.66^{+0.32}_{-0.36}$	$0.07^{+0.03}_{-0.04}$	382^{+164}_{-218}			
IGR J18027−2016	0745060401	OOE	...	...	...	...	...	...	...	...	...
IGR J17252−3616	0405640201	E	$6.40^{+0.03}_{-0.03}$	$0.13^{+0.02}_{-0.03}$	2695^{+415}_{-622}	...	...	...	...	...	...
IGR J17252−3616	0405640601	E	$6.41^{+0.02}_{-0.02}$	$0.18^{+0.04}_{-0.03}$	1831^{+407}_{-305}	...	...	...	...	...	...
IGR J17252−3616	04056401001	E	$6.40^{+0.33}_{-0.27}$	$0.04^{+0.03}_{-0.02}$	921^{+691}_{-460}	...	...	...	...	...	...
IGR J16479−4514	0512180101	E	$6.41^{+0.02}_{-0.02}$	$0.09^{+0.01}_{-0.01}$	803^{+89}_{-89}	...	...	...	$6.88^{+0.23}_{-0.12}$	$0.05^{+0.26}_{-0.18}$	576^{+345}_{-230}
IGR J16418−4532	0679810101	E	$6.43^{+0.04}_{-0.04}$	$0.06^{+0.02}_{-0.02}$	1358^{+453}_{-453}	...	...	...	$6.94^{+0.36}_{-0.27}$	$0.05^{+0.03}_{-0.02}$	1911^{+1146}_{-764}

Note. Line fluxes are given in units of 10^{-4} photons cm^{-2} s^{-1}.

model. The power-law photon index has a negative value (−0.41) during eclipse. In the out-of-eclipse phase, it increases by ∼0.24 and is consistent with the range of (−0.72, 0.35). The total flux in the energy range of (0.3–10) keV is large by ⩾8 times compared to the eclipse phase. During eclipse, the 6.37 keV Fe K$_\alpha$ emission line flux has been found to be 5.96×10^{-4} photons cm^{-2} s^{-1} with a very high equivalent width of $\sim 1258^{+101}_{-103}$ eV. During the out-of-eclipse phase, the flux for the 6.44 keV Fe K$_\alpha$ emission line is found to be 14.88×10^{-4} photons cm^{-2} s^{-1}, which is ∼2.5 times higher than its value during eclipse and the equivalent width decreases by a factor of ∼6.6 to ∼191 eV.

The eclipse spectrum from the second pn observation (OBS ID: 0600950101) has been fitted with a power law modified with a high-energy cutoff, blackbody emission, and 13 Gaussian functions with energies of 0.81, 1.28, 1.75, 1.97, 2.34, 2.57, 2.99, 3.70, 4.12, 6.39, 6.68, 7.05, and 7.49 keV modified by photoelectric absorption. The best fit is obtained with the addition of an edge at 7.06 keV. The power-law photon index is found to have a negative value of −1.34. The value of the high-energy cutoff is determined to be 5.58 keV with a folding energy of 4.59 keV. The fluorescent Fe K$_\alpha$ emission line flux was found to be 4.89×10^{-4} photons cm^{-2} s^{-1} with a very high equivalent width of $\sim 1061^{+13}_{-13}$ eV. The Fe XXV emission line flux was found to be low, 0.26×10^{-4} photons cm^{-2} s^{-1}, with a very small equivalent width of $\sim 22^{+4}_{-3}$ eV. The 7.05 keV emission line flux and equivalent width were found to be 0.88×10^{-4} photons cm^{-2} s^{-1} and $\sim 219^{+25}_{-32}$ eV, respectively.

In the eclipse spectrum of the second pn observation, we detected many emission lines while in the eclipse spectrum of the first observation we detected only one emission line. The eclipse duration covered in the first observation was significantly shorter than that in the second observation. We checked for the upper limits of the emission lines which were not detected in the eclipse spectrum of the first observation, and we found a low upper limit of the equivalent width of those lines.

Table 6
Ratios of the Out-of-eclipse to Eclipse (OOE/E) Fluxes in the 0.3–10 keV Energy Range and Equivalent Widths of Fe Emission Lines

Source	Observation ID	Flux Ratio (0.3–10 keV)	Ratio of Eqv Width (Fluorescent Fe K$_\alpha$)	Ratio of Eqv Width (Fe XXV)	Ratio of Eqv Width (Fe XXVI)
Cen X-3	0111010101	9.79	1.82	0.53	0.66
LMC X-4	0142800101	237.18	⋯	⋯	⋯
LMC X-4	0203500201	86.00	⋯	⋯	⋯
SMC X-1	0011450101	76.62	⋯	⋯	⋯
4U 1700−377	0083280401	8.01	0.15	⋯	⋯
4U 1538−522	0152780201	30.28	0.1	⋯	⋯
IGR J18027−2016	0745060401	43.38	⋯	⋯	⋯

We can say that because of limited statistics, we could not constrain other emission lines in the eclipse phase of the first observation. The emission lines in 4U 1700−377 were discussed by van der Meer et al. (2005). In this work, we restrict our discussion to the Fe lines that are common in most HMXBs.

4U 1538−522: Mukherjee et al. (2006) performed out-of-eclipse spectral analysis of the source with *RXTE* and *BeppoSAX* at two different orbital phases. They obtained the best fit of *RXTE* (3–10 keV) data with a power law with high-energy cutoff and the 6.4 keV Fe K$_\alpha$ emission line modified by photoelectric absorption, while with *BeppoSAX* in the energy range of 0.3–10 keV, they obtained the best fit with the same model except for the high-energy cutoff. They did not see any significant variation of the photon index and Fe line flux over the orbital phase with orbital phase-resolved spectral analysis, while they found a large variation of column densities along the orbital phase, which increases even more just before and after the eclipse asymmetrically. They suggest a nearly constant accretion rate and slightly asymmetric condition of the accretion column due to trailing accreting material from the supergiant. Rodes-Roca et al. (2011) obtained the orbital phase-averaged and eclipse spectra with the same *XMM-Newton* observation of 4U 1538−522. They reported the best fit of the phase-averaged spectra with three absorbed power laws (with same photon indices but different normalizations and column densities) and four Gaussian functions for the fluorescent ∼6.4 keV Fe K$_\alpha$, ∼2.42, ∼1.90, and ∼1.34 keV emission lines. They obtained the best fit for the eclipse spectra with two absorbed power laws and six Gaussian functions for the ∼6.4 keV fluorescent Fe K$_\alpha$, ∼6.63 keV Fe XXV, ∼2.44 keV, ∼2.00 keV, ∼1.85 keV, and ∼1.34 keV emission lines. They identified the low-energy emission lines from different species of sulfur (S), silicon (Si) and magnesium (Mg) ions (Tables 3 and 6; Rodes-Roca et al. 2011). A soft excess was observed below 0.5 keV, which could not satisfactorily explained by either a soft power law or blackbody emission.

The EPIC pn observation of 4U 1538−522 (OBS ID: 0152780201) covers a small part of the out-of-eclipse persistent phase, the eclipse ingress, and the full length of the total eclipse. The eclipse spectrum of this observation is best fitted with a power law, and seven Gaussian functions with energies 1.26, 1.85, 2.40, 6.02, 6.38, 6.69, and 6.95 keV modified by photoelectric absorption. The out-of-eclipse spectrum of this observation has a best fit with a power law and a Gaussian function for the fluorescent Fe K$_\alpha$ emission line together modified by photoelectric absorption along with a less absorbed blackbody emission. The line-of-sight equivalent hydrogen column density associated with the power-law emission is 17.16×10^{22} cm^{-2},

while that for the blackbody emission is found to be 0.54×10^{22} cm^{-2}. This value is less by a factor of more than 30 compared to that for the power-law emission. The power-law photon index in the out-of-eclipse phase increases by ∼0.5, and the total flux in the energy range of (0.3–10) keV is enhanced by a factor of ⩾30 compared to its value in the eclipse phase. Both the eclipse and the out-of-eclipse spectra show the signatures of Fe K$_\alpha$ emission line with fluxes of 0.57×10^{-4} photons cm^{-2} s^{-1} and 2.46×10^{-4} photons cm^{-2} s^{-1} with equivalent widths of 792_{-42}^{+42} eV and 79_{-18}^{+22} eV, respectively. The flux for the Fe K$_\alpha$ emission line increases by a factor of ⩾4, while the equivalent width decreases by a factor of more than 10 in the out-of-eclipse phase from its value in the eclipse phase. Figure 7 shows that the soft X-ray emission in the eclipse and the out-of-eclipse spectra overlaps, and the corresponding flux in the energy range of 0.3–2.0 keV is obtained as 1.76×10^{-13} erg cm^{-2} s^{-1} and 2.08×10^{-13} erg cm^{-2} s^{-1}, respectively. The emission lines in 4U 1538−522 were reported by Rodes-Roca et al. (2011). In this work, we confine our discussion to the Fe lines only.

IGR J18027−2016: Hill et al. (2005) carried out a spectral analysis of IGR J18027−2016 with *INTEGRAL* and *XMM-Newton*. With the simultaneous fitting of both spectra, they obtained a good fit with an absorbed broken power law and a broad Gaussian for the soft excess. The break was found at ∼11 keV, and the power-law photon indices have values of ∼0.8 and ∼3. Addition of 6.4 and 7.1 keV emission lines slightly improves the fit. With pulse-phase-resolved spectroscopy, they found similar spectral parameters, with high values of the line-of-sight hydrogen column densities. These indicate that the absorption is not due to the neutron star's accretion column, and the pulsar is surrounded by the supergiant's dense wind. Aftab et al. (2016) obtained orbital phase-resolved spectroscopy of 33 *Swift*–XRT observations and found a large variation in the source flux, photon index, and equivalent hydrogen column density. This indicates a strongly variable accretion rate of the pulsar and variable wind structures of the supergiant. The detection of several low-intensity states along with high states with *Swift*–XRT suggests clumpy wind structures or hydrodynamic instabilities in the accreted material (Aftab et al. 2016).

The EPIC pn observation of IGR J18027−2016 (OBS ID: 0745060401) covers a major part of the total eclipse, the eclipse egress, and part of the out-of-eclipse phase. The eclipse spectrum of this observation is best fitted with a power law and two Gaussian functions, one for the fluorescent Fe K$_\alpha$ emission line of energy 6.41 keV and another of the highly ionized 6.66 keV Fe XXV emission line, modified by photoelectric absorption. The N_H could not be constrained for the eclipse spectrum. The flux for the Fe K$_\alpha$ emission line is found to be

0.07×10^{-4} photons cm^{-2} s^{-1} with an equivalent width of 445^{+254}_{-191} keV. The best fit for the out-of-eclipse spectrum was obtained with a power law modified by photoelectric absorption only. The power-law photon index in the eclipse phase has been found to be $-0.22^{+0.24}_{-0.23}$, which is consistent with the range of $(-0.02, 0.54)$. In the out-of-eclipse phase, it increases by ~ 1 and becomes positive (0.71). The total flux in the out-of-eclipse phase in the energy range of $(0.3–10)$ keV is increased by a factor of $\geqslant 43$.

IGR J17252−3616: Manousakis & Walter (2011) fitted the orbital phase-resolved *XMM-Newton* spectra with an intrinsically absorbed cutoff power law, a blackbody radiation, and a Gaussian function for the 6.4 keV emission line. The cutoff energy was found to be 8.2 keV with photon index 0.02. The blackbody temperature was 0.5 keV. They also found an Fe K edge at 7.2 keV. They obtained high and variable intrinsic absorbing column densities ($(9–89) \times 10^{22}$ cm^{-2}). The Fe emission line equivalent width was found to be highly variable, in the range of 40–1100 eV. Tawara et al. (1989) found strong and variable absorption of the source by fitting *GINGA* data with an absorbed power law. They found column density up to $\sim 10^{24}$ cm^{-2}. They suggest dense matter surrounding the pulsar. With *GINGA* data, taken ~ 6 months later, Takeuchi et al. (1990) found a lower value of the column density ($\sim 10^{23}$ cm^{-2}), fitting the spectrum with a power-law modified with high-energy cutoff. Pulse-phase-resolved spectroscopy of the source with *INTEGRAL* obtained by Zurita Heras et al. (2006) shows nearly the same continuum emission. Thompson et al. (2007) fitted several orbital phase-resolved *RXTE* spectra including eclipse with an absorbed power law modified by a high-energy cutoff and a Gaussian function for the 6.4 keV Fe emission line. They obtained a cutoff of ~ 16 keV for the best fit. They obtained column densities in the range of $(8–126) \times 10^{22}$ cm^{-2}, photon indices in the range of 0.5–2, and huge variation in the 6.4 keV Fe emission line equivalent width (133–6490 eV).

We analyzed three EPIC pn observations of IGR J17252−3616, all during eclipse phases observed between 2006 August 29–September 27 (OBS IDs: 0405640201, 0405640601, 0405641001). All three observations were initially fitted with a power law modified by photoelectric absorption. For the best fit, the first observation needed two Gaussian functions and a less absorbed blackbody emission. One Gaussian is for the Fe K$_\alpha$ emission line of 6.4 keV and another with a value of 7.01 keV. The second observation was best fitted with the same model as the first observation, except the Gaussian with a value of 7.01 keV. The third observation obtained the best fit with a Gaussian function for the Fe K$_\alpha$ emission line of energy 6.4 keV. The soft excess in this observation could not be fitted with blackbody emission. The power-law photon index is found to have values of $0.24^{+0.83}_{-0.75}$, $0.81^{+4.92}_{-1.17}$, and $-0.52^{+4.35}_{-2.47}$, respectively, in the three observations, while the Fe K$_\alpha$ emission line flux is 0.13, 0.18, and 0.04, respectively, in units of 10^{-4} photons cm^{-2} s^{-1}. The equivalent width is found to be significantly different for the three observations with values of 2695^{+415}_{-622} eV, 1831^{+407}_{-305} eV, and 921^{+691}_{-460} eV, respectively. The flux and equivalent width associated with the 7.01 keV emission line is 0.05×10^{-4} photons cm^{-2} s^{-1} and 1227^{+982}_{-245} eV, respectively, in the first observation. This is significant at $\gtrsim 3\sigma$. We could not detect this line in the other two observations, as the data are not that good. The line-of-sight equivalent hydrogen column density for the power-law component for the three observations is 9.34, 18.17, and 13.48, respectively,

while that for the blackbody component is 0.90 and 2.67 for the first two observations, respectively (all values in units of 10^{22} cm^{-2}), which are lower compared to the same for the power-law component by a factor of >10 and ~ 7, respectively.

IGR J16479−4514: Romano et al. (2009) fitted the out-of-outburst *Swift*–XRT data with an absorbed power law plus blackbody emission. They suggest a small region on the neutron star surface, perhaps the polar cap, as the origin of the blackbody emission. Sidoli et al. (2013) observed the source with *Suzaku* in the eclipse and out-of-eclipse phases. They fitted all of the spectra with an absorbed power law and 6.4 keV Fe emission line. They found a hard power law when the source is brighter, like other SFXTs and HMXB pulsars. The line-of-sight column density did not show much variation outside the eclipse. The Fe line flux was observed to vary throughout the orbit with a correlation with the unabsorbed source flux above 7 keV. The Fe line equivalent width was found to increase during eclipse as expected.

The EPIC pn observation of IGR J16479−4514 (OBS ID: 0512180101) covers the eclipse ingress and a major part of the total eclipse. We extracted only the eclipse spectrum from the total eclipse event for this observation. The eclipse spectrum of this observation is best fitted with a power law, two Gaussian functions with energies 6.41 and 6.88 keV modified by photoelectric absorption, and a less absorbed blackbody emission associated with the line-of-sight equivalent hydrogen column density of 0.58×10^{22} cm^{-2}, which is a factor of ~ 8 lower than that associated with the power law. The power-law photon index is obtained to be $1.28^{+0.37}_{-0.34}$. The Fe K$_\alpha$ emission line flux is low with a value of 0.09×10^{-4} photons cm^{-2} s^{-1} and equivalent width of 803^{+89}_{-89} eV. The energy value for the 6.88 keV emission line is not well constrained like the Fe XXVI emission line for other observations (please see Table 5), and the flux for this emission line is 0.05×10^{-4} photons cm^{-2} s^{-1} with an equivalent width of 576^{+345}_{-230} eV.

IGR J16418−4532: Romano et al. (2012) obtained the best fit of *Swift*–XRT out-of-eclipse spectra with a single absorbed power law. They obtained high intrinsic absorption (up to $\sim 7 \times 10^{22}$ cm^{-2}). The spectral parameters did not show much variation though the flux variation was quite large. Average spectra based on 2004 and 2011 *XMM-Newton* data were well fitted with an absorbed power-law model (Sidoli et al. 2012a). The 2004 data showed marginal evidence of a soft excess below 2 keV. They did not find clear evidence of any Fe emission line. The eclipse spectrum with *INTEGRAL* was fitted with a simple power law with a photon index of 2.2 (Drave et al. 2013b). The best fit of the mid-eclipse spectrum with *XMM-Newton* was obtained with an absorbed power law and two Gaussian functions for the 6.4 and 6.65 keV Fe emission lines. The post-eclipse spectra did not show any evidence of an Fe emission line (Drave et al. 2013b).

The EPIC pn observation of IGR J16418−4532 (OBS ID: 0679810101) covers a major part of the total eclipse. So, for this observation, we extracted the eclipse spectrum only, which has been fitted with a power law and two Gaussian functions, one for the fluorescent Fe K$_\alpha$ emission line of 6.43 keV and another for the highly ionized Fe XXVI emission line of 6.94 keV, modified by photoelectric absorption. The power-law photon index has been found to be $0.40^{+0.83}_{-0.45}$. The Fe K$_\alpha$ emission line flux is 0.06×10^{-4} photons cm^{-2} s^{-1} with a high equivalent width of 1358^{+453}_{-453} eV. The Fe XXVI emission line

Aftab, Paul, & Kretschmar

Table 7
Emission Line Energy, Flux, and Equivalent Width for Emission Lines Other than Fe

Source Name (OBS ID)	Line Energy (keV)	Phase	Emission Line Flux	Emission Line Eqv. Width (eV)	Line Identification	Previous Detection (keV, Line)
Cen X-3 (0111010101)	$0.98^{+0.01}_{-0.02}$	E	$10.5^{+5.5}_{-3.6}$	96^{+50}_{-33}	Ne X	1.022, Ne X (eclipse) (v1); 1.022, Ne X (All phase ranges) (v2)
	$1.43^{+0.02}_{-0.02}$	E	$0.83^{+0.27}_{-0.25}$	37^{+12}_{-11}	Mg XII	1.472, Mg XII (All phase ranges) (v2)
	$1.98^{+0.01}_{-0.02}$	E	$1.24^{+0.25}_{-0.20}$	102^{+20}_{-16}	Si XIV and/P $K_{\alpha1}, K_{\alpha2}$	2.00 ± 0.01, Si XIV (eclipse) (v1)
	$2.62^{+0.01}_{-0.02}$	E	$0.91^{+0.15}_{-0.11}$	94^{+15}_{-11}	Cl $K_{\alpha1}, K_{\alpha2}$ and/Si XVI	2.64 ± 0.02, Si XVI (eclipse) (v1); 2.621, S XVI (All phase ranges) (v2)
	$3.34^{+0.04}_{-0.04}$	E	$0.29^{+0.08}_{-0.08}$	35^{+10}_{-10}	K $K_{\alpha1}, K_{\alpha2}$	...
	$1.34^{+0.04}_{-0.06}$	OOE	$65.47^{+24.06}_{-18.12}$	345^{+127}_{-95}	Mg $K_{\beta1}$	...
	$1.79^{+0.03}_{-0.03}$	OOE	$12.23^{+3.27}_{-2.65}$	114^{+30}_{-25}	Si $K_{\alpha1}, K_{\alpha2}, K_{\beta1}$	1.79 ± 0.05, Si I and or Si XIII (pre-eclipse) (v1)
	$2.02^{+0.01}_{-0.01}$	OOE	$5.51^{+0.89}_{-1.1}$	53^{+9}_{-11}	Si XIV and/P $K_{\alpha1}, K_{\alpha2}$	1.99 ± 0.02, Si XIV (pre-eclipse) (v1); 2.006, Si XIV (All phase ranges) (v2)
	$2.64^{+0.02}_{-0.02}$	OOE	$2.48^{+0.39}_{-0.40}$	29^{+5}_{-5}	Cl $K_{\alpha1}, K_{\alpha2}$ and/Si XVI	2.64 (fixed), Si XVI (pre-eclipse) (v1); 2.621, S XVI (All phase ranges) (v2)
	$6.19^{+0.15}_{-0.19}$	OOE	$10.41^{+2.39}_{-2.80}$	133^{+31}_{-36}	...	...
LMC X-4 (0142800101)	$0.96^{+0.01}_{-0.01}$	OOE	$7.36^{+0.05}_{-0.05}$	29^{+0}_{-0}	Cu L_{β}/ Zn L_{α}	0.91434 keV (13.560 Å), Ne IX He$_{\alpha}$ (w1) 1.01977 keV (12.158 Å), Ne X Ly$_{\alpha}$ (w1)
LMC X-4 (0203500201)	$0.98^{+0.03}_{-0.03}$	OOE	$5.65^{+2.02}_{-1.54}$	34^{+12}_{-9}	Cu L_{β}/ Zn L_{α}	0.91434 keV (13.560 Å), Ne IX He$_{\alpha}$ (w1) 1.01977 keV (12.158 Å), Ne X Ly$_{\alpha}$ (w1)
4U 1700–377 (0600950101)	$0.81^{+0.10}_{-0.13}$	E	$8.11^{+32.5}_{-3.95}$	90^{+359}_{-44}	Ne K_{α}, O VIII RRC	0.86 ± 0.02, Ne K_{α}, O VIII RRC (eclipse) (x1)
	$1.28^{+0.05}_{-0.05}$	E	$2.05^{+0.07}_{-0.40}$	1208^{+41}_{-236}	Mg $K_{\alpha1}, K_{\alpha2}, K_{\beta1}$	1.30 ± 0.01, Mg K_{α}, Mg XI He$_{\alpha}$ (eclipse) (x1)
	$1.75^{+0.01}_{-0.01}$	E	$0.87^{+0.14}_{-0.11}$	898^{+144}_{-113}	Si $K_{\alpha1}, K_{\alpha2}$/Al XIII Ly$_{\alpha}$	1.75 ± 0.01, Si K_{α}, Al XIIILy$_{\alpha}$ (eclipse) (x1)
	$1.97^{+0.03}_{-0.03}$	E	$0.16^{+0.03}_{-0.03}$	139^{+26}_{-26}	Si XIV Ly$_{\alpha}$	2.00 ± 0.01, Si XIV Ly$_{\alpha}$ (eclipse) (x1)
	$2.34^{+0.01}_{-0.01}$	E	$0.52^{+0.06}_{-0.05}$	392^{+45}_{-38}	S K_{α}, Al XIII RRC	2.33 ± 0.01, S K_{α}, Al XIII RRC (eclipse) (x1)
	$2.57^{+0.05}_{-0.06}$	E	$0.08^{+0.02}_{-0.02}$	54^{+14}_{-14}	Cl $K_{\alpha1}, K_{\alpha2}$/ S XVI Ly$_{\alpha}$, Si XIV RRC	2.63 ± 0.01, S XVI Ly$_{\alpha}$, Si XIV RRC (eclipse) (x1)
	$2.99^{+0.01}_{-0.01}$	E	$0.21^{+0.02}_{-0.02}$	115^{+11}_{-11}	Ar $K_{\alpha1}, K_{\alpha2}$	2.97 ± 0.01, Ar K_{α} (eclipse) (x1)
	$3.70^{+0.01}_{-0.01}$	E	$0.25^{+0.03}_{-0.03}$	102^{+12}_{-12}	Ca $K_{\alpha1}, K_{\alpha2}$	3.71 ± 0.01, Ca K_{α} (eclipse) (x1)
	$4.12^{+0.05}_{-0.05}$	E	$0.08^{+0.02}_{-0.02}$	29^{+7}_{-7}	Sn $L_{\gamma1}$/Sb $L_{\beta2}$ / Xe L_{α}/Sc $K_{\alpha1}, K_{\alpha2}$	...
	$7.05^{+0.02}_{-0.01}$	E	$0.88^{+0.10}_{-0.13}$	219^{+25}_{-32}	Fe $K_{\beta1}$	...
	$7.49^{+0.02}_{-0.02}$	E	$0.29^{+0.06}_{-0.05}$	71^{+15}_{-12}	Co $K_{\beta1}$, Ni $K_{\alpha1}, K_{\alpha2}$	...
4U 1538−522 (0152780201)	$1.26^{+0.05}_{-0.07}$	E	$0.22^{+0.07}_{-0.04}$	321^{+102}_{-58}	Mg $K_{\alpha1}, K_{\alpha2}, K_{\beta1}$	1.34 (fixed), Mg K_{α}, Mg XI He$_{\alpha}$ (eclipse) (y1)

Table 7
(Continued)

Source Name (OBS ID)	Line Energy (keV)	Phase	Emission Line Flux	Emission Line Eqv. Width (eV)	Line Identification	Previous Detection (keV, Line)
	$1.85^{+0.03}_{-0.03}$	E	$0.15^{+0.02}_{-0.02}$	250^{+33}_{-33}	Si $K_{\beta1}$	$1.848^{+0.012}_{0.024}$, Si XIII Heα (eclipse) (y1)
	$2.40^{+0.04}_{-0.03}$	E	$0.07^{+0.01}_{-0.01}$	116^{+17}_{-17}	S $K_{\beta1}$	$2.4427^{+0.0023}_{0.023}$, S XV Heα (eclipse) (y1)
	$6.02^{+0.05}_{-0.05}$	E	$0.04^{+0.01}_{-0.01}$	54^{+14}_{-14}	Cr $K_{\beta1}$	⋯
IGR J17252−3616 (0405640201)	$7.01^{+0.14}_{-0.40}$	E	$0.05^{+0.04}_{-0.01}$	1227^{+982}_{-245}	⋯	⋯

Note. Line fluxes are given in units of 10^{-4} photons cm^{-2} s^{-1}. (v1): Ebisawa et al. (1996), (v2): Wojdowski et al. (2001), (w1): Neilsen et al. (2009), (x1): van der Meer et al. (2005), (y1): Rodes-Roca et al. (2011).

flux has been found to be 0.05×10^{-4} photons cm^{-2} s^{-1} with equivalent width of 1911^{+1146}_{-764} eV.

Emission lines other than Fe K$_\alpha$: We observed emission lines other than Fe K$_\alpha$ in Cen X-3, LMC X-4, 4U 1700–377, 4U 1538–522, and IGR J17252–3616. The line parameters and their previous detections are given in Table 7. Some of the emission lines were not observed earlier. However, in this work, we focus our discussion on Fe emission lines only, so details of other emission lines are not discussed here.

3. Discussion

During the X-ray eclipses, direct emission from the compact object is blocked by the companion and the observed X-rays during eclipses are the reprocessed emission of the primary X-rays from the surrounding medium. For HMXBs, the main reprocessing agent is the stellar wind of the companion and any structures in the wind, if present. The best-fit models for all sources are given in Table 3. Among the multiple spectral components, the continuum is expected to be strongly suppressed during the eclipses, and the emission lines which are often produced in a larger region in the stellar wind are expected to be suppressed to a lesser extent. The eclipse spectrum is therefore expected to show a larger equivalent width and better detectability of the emission lines compared to the out-of-eclipse spectrum. However, depending on the distribution of the material around the compact object and the wind density, this effect can be different in different sources. To investigate the phenomenon of X-ray reprocessing in the stellar wind in a large number of HMXBs, and to find if there are significant system to system differences, we analyzed 13 eclipse observations of nine HMXBs with out-of-eclipse observations, whenever these are available along with eclipse phases in the same observation. We then compared the eclipse spectra of these sources and also compared the eclipse and out-of-eclipse spectra whenever available. We found some similarities and significant differences in the reprocessing properties of the HMXB systems we analyzed. All of these HMXBs have supergiant companions with stellar mass in the range of $\sim16\,M_\odot$ to $52\,M_\odot$, radius in the range of $8\,R_\odot$ to $26\,R_\odot$, and orbital period of binaries in the range of 1.41–9.74 days. Accretion in three of these systems, LMC X-4, Cen X-3, and SMC X-1 are at least in parts due to Roche lobe overflow (Savonije 1978; van der Meer et al. 2007).

A summary of the comparison of various aspects of the X-ray reprocessing in these HMXBs is as follows: the equivalent width of the low-ionization (or neutral) Fe K$_\alpha$ emission line during eclipse is found to have a wide range, from $\sim126^{+18}_{-18}$ eV (in SMC X-1, OBS ID: 0011450101) to 2695^{+415}_{-622} eV (in IGR J17252−3616, OBS ID: 0405640201) i.e., a factor of >20 larger in the latter source. The ratio of the equivalent widths of these Fe K$_\alpha$ emission lines during the eclipse and the out-of-eclipse phases also have a large range, from ~0.55 (in Cen X-3) to ~10 (in 4U 1538−522). We compared the best-fit models in the energy range of 0.3–10 keV and 3–10 keV. We found consistent values of the equivalent widths of the Fe lines in eclipse and out-of-eclipse phases. So, the errors quoted for the equivalent widths are statistical errors only; these do not depend on the choice of continuum. The flux ratio of the eclipse to out-of-eclipse spectra has a wide range, from ~8 (in 4U 1700−377, OBS ID: 0083280401) to ~237 (in LMC X-4, OBS ID: 0142800101), which differs by a factor of ~30. Even in the same source LMC X-4, the ratio of the flux in the out-of-eclipse to the eclipse phase varies by as much as a factor of ~3 (from ~237 to ~86) in different observations. Here we discuss the results of some individual sources.

3.1. Cen X-3

In Cen X-3 (OBS ID: 0111010101), three Fe emission lines i.e., the 6.41 keV (fluorescent Fe K$_\alpha$), 6.66 keV (Fe XXV), and 6.94 keV (Fe XXVI) emission lines were detected. The equivalent widths of the Fe XXV and Fe XXVI emission lines were observed to be higher in the eclipse compared to the out-of-eclipse phase as expected. The equivalent width of the Fe emission lines in this source during eclipse is smaller than that for other SgHMXBs with a similar line-of-sight equivalent hydrogen column density (N_H). Ebisawa et al. (1996) and Naik & Paul (2012) also found a lower equivalent width of Fe emission lines in the eclipse compared to the out-of-eclipse phase with *ASCA* and *XMM-Newton*, respectively. The wind in Cen X-3 is smooth (Wojdowski et al. 2001). A low-density wind in the surrounding region of the compact object can produce a low equivalent width, but why the O-type supergiant companion in Cen X-3 has a thinner wind than O- and B-type supergiants in other HMXB systems is not understood. The equivalent width of the Fe K$_\alpha$ emission line was found to be lower in the eclipse phase compared to the out-of-eclipse phase

as observed by Naik & Paul (2012) and Ebisawa et al. (1996). The Fe K_α emission line flux increases by a factor of more than 17 as the source comes out of the eclipse, while the Fe XXV and Fe XXVI emission line fluxes increase by a factor of ∼5.5 and ∼5.8, respectively. A similar result was obtained by Naik & Paul (2012). These observations confirm that most of the fluorescent Fe K_α line-emitting region was closer to the source and distributed in a region of size comparable to or smaller than the radius of the companion star from the compact object. The ionization state of the Fe atoms are expected to be high near the compact object because of its intense X-ray emission, but here we see most of the low-ionization Fe atoms are closer to the compact object compared to the highly ionized Fe atoms. This is possible if the Fe atoms closer to the source are in a very dense optically thick accretion disk or in a dense accretion stream. The high density of the disk or the stream keeps the Fe atoms lowly ionized in spite of them being near the source.

3.2. LMC X-4

Naik & Paul (2004b) observed the source in the low and high states of its superorbital period with *BeppoSAX*. The decrease of the continuum flux was found to be by more than a factor of 5 compared to the decrease of the 6.4 keV Fe line flux in the low state, which they suggest is caused by the different origins of the continuum and the Fe line emission. The smaller value of the Fe line flux and the higher value of Fe line equivalent width in the low state indicates that a major part of the line emission is from a region comparable to or smaller than the size of the obscuring material (most probably part of the accretion disk) and also that some part of the emission line comes from an extended region. In the low state, they did not find any significant increase of the line-of-sight column density, indicating that the continuum X-ray emission comes from an extended region. The equivalent width of the fluorescent Fe K_α emission line was detected during the low and high states of the source with 1260 eV and 240 eV, respectively. Neilsen et al. (2009) found a variable Doppler shift of the Fe lines. They suggest that the origin of the Fe line is the inner accretion disk warp. The evolution of the other emission lines suggests precession of the accretion disk.

During the eclipse in the first pn observation of LMC X-4 (OBS ID: 0142800101), the fluorescent Fe K_α emission line was detected with a high equivalent width (597^{+171}_{-256} eV), but this line is absent in the out-of-eclipse phase. The large increase (>237 times) of the total flux in the out-of-eclipse phase perhaps strongly suppressed this emission line, which makes it undetectable during the out-of-eclipse phase. The Fe XXV emission line was detected during the out-of-eclipse phase but it is absent in the eclipse phase, which indicates that most of the highly ionized wind material which emits Fe XXV photons is distributed in a region smaller than the distance comparable to the radius of the companion from the compact object. In the second observation of LMC X-4 (OBS ID: 0203500201) during the eclipse, the detection of the fluorescent Fe K_α emission line is marginal. However, we cannot rule out this line as the statistics of the eclipse spectrum of this observation is very poor. During the out-of-eclipse phase in the second observation, the fluorescent Fe K_α emission line is comparatively stronger. This indicates that most of the lowly ionized Fe atoms were closer to the source during this observation. When the source came out of the eclipse, these Fe atoms showed their presence through the 6.38 keV emission line during the

out-of-eclipse phase. This can happen only if these Fe atoms are in the dense accretion disk and/or accretion stream during this observation. The highly ionized 6.99 keV Fe XXVI emission line was also detected during the out-of-eclipse phase of the second observation, but it is insignificant in the eclipse phase, which possibly indicates that the origin of this emission line is very near the compact object. However, due to poor statistics of the eclipse spectrum, we cannot make any definitive comment about the scenario. The highly ionized Fe XXVI emission line has been detected in LMC X-4 for the first time (OBS ID: 0203500201). None of the earlier observations detected this emission line in this source. We checked for the superorbital phase of the source during the out-of-eclipse phase of this observation and found it in the bright phase, while the other observation (OBS ID: 0142800101) of this source shows a low superorbital phase. During the eclipse phase in the first observation of LMC X-4, the total flux (0.3–10.0 keV) is lowered by a large factor (>237) from the out-of-eclipse phase, while in the second observation, the flux ratio between the out-of-eclipse to the eclipse phase is ∼86. This signifies a difference in the density and/or spatial distribution of the reprocessing material between these two observations. During the eclipse in the first observation, the low-ionization (or neutral) fluorescent 6.36 keV Fe K_α emission line was detected, while in the second observation during the eclipse phase, the detection of this line is insignificant. In the first observation during the out-of-eclipse phase among Fe emission lines, only the highly ionized 6.60 keV Fe XXV emission line was detected; in the second observation during the out-of-eclipse phase, the 6.38 keV Fe K_α emission line and highly ionized 6.99 keV XXVI emission line were detected. These indicate higher ionization of matter near the compact object during the second observation compared to the first observation. Low-ionization (or neutral) 6.38 keV Fe K_α and highly ionized Fe XXVI emission during the out-of-eclipse phase of the second observation indicate a mixture of hot and cold wind near the compact object. Low-ionization Fe atoms could possibly be distributed in the optically thick accretion disk or in the dense accretion stream closer to the source. The high density of the stream makes them low-ionized despite these Fe atoms being near the source.

3.3. 4U 1700−377

In all eclipse, eclipse egress, and low-flux spectra of 4U 1700−377, van der Meer et al. (2005) found a ∼6.4 keV Fe emission line; they suggest a clumpy wind near the compact object as the origin of this line. The detection of many strong emission lines during eclipse indicates that these lines are originating from an extended region. Also, the intensity of some of the emission lines with very high values of ionization parameters increase toward egress, which indicates that the extension of the ionized plasma around the central source is not very large either.

Two observations of 4U 1700−377 were separated by a span of more than 8 yr. In the first observation of 4U 1700−377 (OBS ID: 0083280401), low-ionization fluorescent Fe K_α emission line was detected in both the eclipse and out-of-eclipse phases (6.37 keV and 6.44 keV, respectively), which are consistent with the energy of 6.4 keV. The equivalent width of this Fe emission line during eclipse is found to be much higher as compared to that in the out-of-eclipse phase, as expected. The emission flux and the equivalent width of this Fe

K_α emission line detected during eclipse are found to be higher compared to the same in the other observation (OBS ID: 0600950101) during eclipse. This signifies greater reprocessing by low-ionization Fe atoms during this observation compared to the later one. Nondetection of Fe XXV and Fe XXVI emission lines in this observation indicates comparatively colder wind during this observation. Many low-energy emission lines were detected in the eclipse spectrum of the second observation but were not detected in the eclipse phase of the first observation, which could be due to limited statistics.

The second observation of 4U 1700−377 (OBS ID: 0600950101) covers only the eclipse, and in this phase, fluorescent Fe K_α and highly ionized Fe XXV emission lines were detected along with other low-energy emission lines and an emission line of energy 7.05 keV. This 7.05 keV emission line could be the Fe K_β line. The ratio of the flux of the Fe K_β to the Fe K_α emission line is 0.18(η). This indicates ionized medium surrounding the compact object ($\eta \leqslant 0.125$ for Fe neutral gas; Kaastra & Mewe 1993), which is consistent with the detection of the highly ionized Fe K_α (Fe XXV) emission line. The equivalent width of the fluorescent Fe K_α emission line is very high (1061^{+13}_{-13} eV) and that of the Fe XXV emission line is quite low (22^{+4}_{-3} eV) in this observation. This indicates an ionized medium; most of the Fe atoms with lower ionization than Fe X are distributed at least at a distance from the compact object comparable to the radius of the companion star during this observation.

3.4. Other Sources

Pulse-phase-resolved spectra of SMC X-1 with *BeppoSAX* show a phase shift of the pulsating soft component compared with the hard power-law component (Naik & Paul 2004a). This suggests different origins of the soft and hard X-rays.

In SMC X-1, a weaker, low fluorescent 6.38 keV Fe K_α emission line was detected with EPIC pn during eclipse with an equivalent width of 126^{+18}_{-18} eV, which is the lowest equivalent width of the fluorescent Fe K_α emission line among all the eclipsing sgHMXBs reported in this work. The detection of this line is marginal in the out-of-eclipse phase (with an upper limit of the equivalent width of ∼90 eV). Despite having good statistics in the eclipse spectra, a weak detection of the fluorescent Fe K_α emission line could be due to the low metallicity of the system.

In the eclipse spectrum of 4U 1538−522 with *XMM-Newton*, Rodes-Roca et al. (2011) found the 6.4 keV Fe K_α fluorescent and 6.6 keV Fe XXV emission line. They also detected other emission lines with a wide range of ionization states. This broad range suggests that the emitting region is either wide or the emitting material has a large range of densities. The coexistence of a variety of recombination and fluorescent emission lines was also observed in Vela X-1 during eclipse with *ASCA* and *Chandra* (Sako et al. 1999; Schulz et al. 2002), which suggests an inhomogeneous wind structure with cool, dense clumps scattered in highly ionized plasma.

In 4U 1538−522, the fluorescent Fe K_α emission line was observed in both the eclipse and the out-of-eclipse phases with a greater equivalent width during the eclipse phase as expected. As pointed out in Section 2.2.1, the power-law component in this source is heavily absorbed, with a column density of $17.16^{+1.17}_{-1.12} \times 10^{22}$ cm^{-2}. A blackbody component should not be detectable, if it has the same column density. We therefore fitted the soft excess with a different column density. The line-of-sight hydrogen column density for the soft excess is less than that for the power law by a large factor (>30), which indicates that soft X-ray emissions are coming from a different region away from the neutron star. Again, the nearly equal soft X-ray fluxes (0.3–2.0 keV) in the eclipse and out-of-eclipse spectra indicate that the origin of the soft X-rays is far away (at least farther away compared to the size of the companion) from the compact object and is not blocked during eclipse.

Hill et al. (2005) obtained a smaller value of the equivalent width of the Fe K_α emission line for IGR J18027−2016 off and on pulse (40 eV and 25 eV, respectively). We detected this Fe emission line with a high equivalent width during eclipse (445^{+254}_{-191} eV) in IGR J18027−2016, but it was not detected in the out-of-eclipse phase, which is similar to the observation of SMC X-1 except that the equivalent width in the case of SMC X-1 during the eclipse phase was found to be low (126^{+18}_{-18} eV).

The observations of IGR J16479−4514 and IGR J16418 −4532, and the three observations of IGR J17252−3616 covered only the eclipse. In these observations, low-ionization (or neutral) Fe K_α emission lines were detected with large equivalent widths. In the first observation (OBS ID: 0405640201) of IGR J17252−3616, the equivalent width is found to be largest (2695^{+415}_{-622} eV) among all the observations analyzed in this work. The varying equivalent width (921–2695 eV) and flux (0.04–0.18 photons cm^{-2} s^{-1}) of the Fe K_α emission line in three observations of IGR J17252−3616 indicates a change in the distribution and density of low-ionization Fe atoms surrounding the compact object at least at a distance equal to the radius of the companion over a period of 1 month. Manousakis & Walter (2011) found spectral variation over the orbital phase of IGR J17252−3616 with *XMM-Newton*. During the eclipse, they found that the equivalent width of the fluorescent Fe K_α emission line dropped by a factor >10, which indicates a cocoon-like wind structure surrounding the compact object. For IGR J16479−4514, Sidoli et al. (2013) also obtained a high equivalent width (5500^{+4500}_{-3700} eV) of the fluorescent Fe K_α emission line during the eclipse with *Suzaku*, while it is in the range of 40–280^{+160}_{-160} eV outside of the eclipse. Using *XMM-Newton* data, Sidoli et al. (2012a) obtained a high Fe K_α emission line equivalent width of 3100 eV during the eclipse.

In the out-of-eclipse phase of the observation of 4U 1538 −522, and also in the eclipse phase of IGR J16479−4514 and in the first two observations of IGR J17252−3616, the line-of-sight equivalent hydrogen column density for the soft X-ray emission is lower by several factors (∼8–680) than that for the power law. This signifies a different origin for the hard and soft X-rays in these sources during the observations mentioned above. Detection of a soft excess, even when the power-law component is absorbed by a very large column density of material (∼10^{24} cm^{-2}), is known in some HMXBs (GX 301-2: Islam & Paul 2014), and it has been attributed to a different origin of the soft component compared to the power-law component.

To study the variation of the X-ray reprocessing with the orbital parameters of the HMXBs, we show the orbital period of the system, mass, radius, mass-loss rate of the companion (through wind), and the projected semimajor axis of the system as functions of the out-of-eclipse to eclipse flux ratios (Figure 14). We did not notice any correlation of these parameters with the flux ratios. In the two observations of LMC X-4, the flux ratios vary by a factor of ∼3. In Figure 15, we show a relation between the equivalent width (Eqw) of the Fe
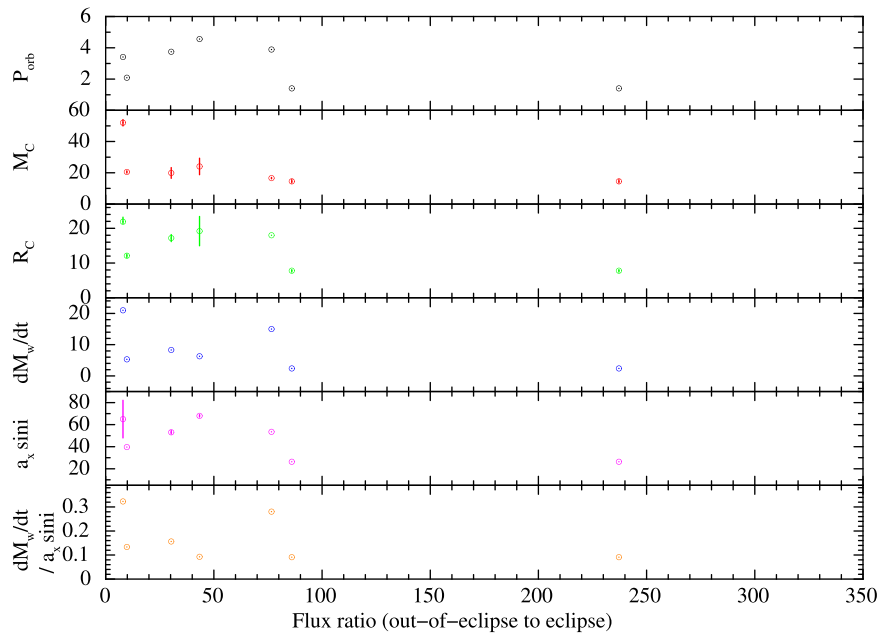
Figure 14. Plot of the different orbital parameters of the eclipsing HMXBs with the out-of-eclipse to eclipse flux ratios. P_{orb}: orbital Period (days), M_C: mass of the companion ($M_\odot$), R_C: radius of the companion star ($R_\odot$), $\dot{M}_w$: mass-loss rate of the companion star ($10^{-7}\ M_\odot\ yr^{-1}$), $a_x \sin i$: projected length of the semimajor axis of the system in the plane along the line of sight (light-second). $M_\odot$, $R_\odot$: mass and radius of the Sun, respectively.

K_α emission line and the line-of-sight equivalent hydrogen column density (N_H) obtained during the out-of-eclipse phase. We do not see an evident correlation between the two parameters. A direct correlation is expected between Eqw and N_H during the out-of-eclipse phase, as this line is produced by the fluorescence of X-rays from the compact object where the surrounding medium causes this fluorescence (George & Fabian 1991). Thus, in a denser surrounding medium, more fluorescence is expected to occur. A direct correlation was observed between the two parameters by Torrejón et al. (2010b) and Giménez-García et al. (2015). Out of the seven out-of-eclipse observations, we detected the fluorescent Fe K_α emission line in four observations. In Figure 15, we also show the upper limit of the equivalent width of the 6.4 keV emission line in three other out-of-eclipse observations. The limited data do not allow a clear conclusion about the relationship between Eqw and N_H in SgHMXB systems.

In Figure 16, we have plotted N_H for the observations that have both eclipse and out-of-eclipse data. In this figure, the X axis indicates the observations and the Y axis in the top panel shows N_H during the eclipse (pink boxes) and out-of-eclipse (blue triangles) phases. The Y axis in the bottom panel gives the value of 0.3–10 keV for the out-of-eclipse to eclipse flux ratios. For three observations (4U 1700−377, OBS ID: 0083280401; 4U 1538−522, and IGR J18027−2016), N_H is larger during the eclipse than during the out-of-eclipse phase. For the other four observations, N_H is comparable in both the phases. In Figure 17, we plot the out-of-eclipse to eclipse flux ratios with the ratio of the line-of-sight equivalent hydrogen column densities (N_H) during the out-of-eclipse and eclipse phases of the HMXBs, for which both out-of-eclipse and eclipse data were available. We excluded LMC X-4 from this plot as the N_H could not be constrained for this source. The sources that show a large flux ratio between the out-of-eclipse and eclipse spectra (SMC X-1, IGR J18027−2016, and 4U 1538−522) probably have a less dense wind environment compared to the two sources Cen X-3 and 4U 1700−377, as the large out-of-eclipse
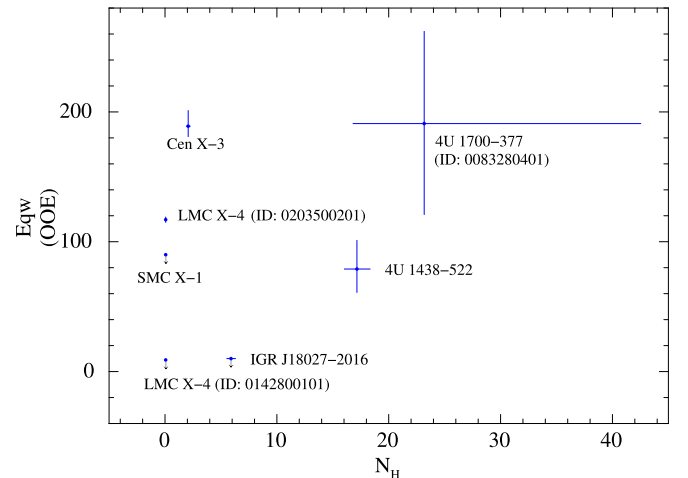

Figure 15. Equivalent width (Eqw, along the Y axis) vs. line-of-sight equivalent hydrogen column density (N_H, along the X axis) of the fluorescent Fe K_α emission line in the out-of-eclipse (OOE) phase. This line is detected in Cen X-3, LMC X-4 (ID: 0203500201), 4U 1700−477 (ID: 0083280401), and in 4U 1538−522, whereas the upper limit of the equivalent width is shown in SMC X-1, LMC X-4 (ID: 0142800101), and IGR J18027−2016. Unfortunately, one cannot correlate between N_H and the equivalent width of the fluorescent Fe K_α emission line in this sample of SgHMXBs, due to the limitation of the available data.

to eclipse flux ratio indicates lesser reprocessing. Within each type, the sources with low ratio of the column density in the out-of-eclipse and eclipse spectra (SMC X-1 and Cen X-3) probably have a more isotropic wind pattern compared to the sources for which the column density is much larger in the out-of-eclipse spectra (4U 1700−377, IGR J18027−2016, and 4U 1538−522). In the latter sources, the supergiant companion might have a stronger wind outflow in the equatorial (or near-equatorial) plane (as shown in Figure 18); the companion could also have a trailing wind, which was described by Blondin (1994) as the shadow wind. These features may explain the
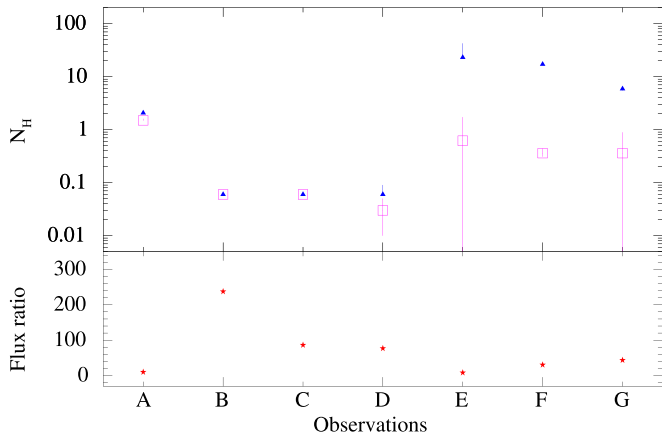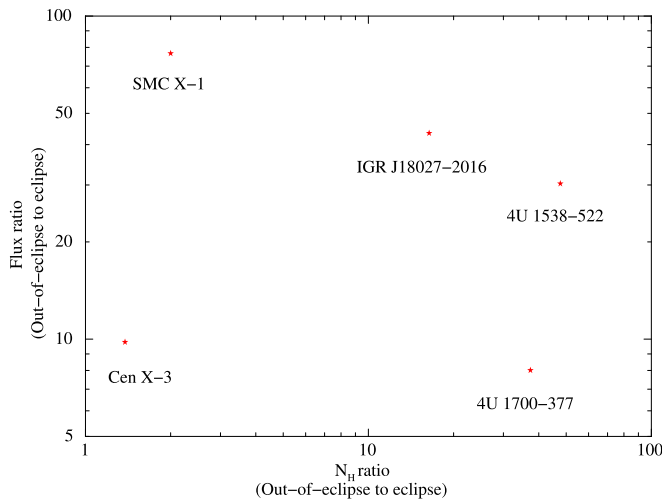
Figure 16. Line-of-sight equivalent hydrogen column density (N_H) of HMXBs during the eclipse and out-of-eclipse phases for observations having data for both phases. The X axis gives the observations, and the Y axis in the top panel shows N_H (eclipse: pink boxes, out-of-eclipse: blue triangles). The Y axis in the bottom panel gives the value of 0.3–10 keV for the out-of-eclipse to eclipse flux ratio. A: Cen X-3. B: LMC X-4, OBS ID: 0142800101. C: LMC X-4, OBS ID: 0203500201. D: SMC X-1. E: 4U 1700−377, OBS ID: 0083280401. F: 4U 1538−522. G: IGR J18027−2016. For three observations (4U 1700−377 OBS ID: 0083280401, 4U 1538−522, and IGR J18027−2016), N_H is larger during the eclipse than during the out-of-eclipse phase. For the other four observations, N_H is comparable in both phases.

Figure 17. Variation of the out-of-eclipse to eclipse flux ratio with the corresponding ratio of the line-of-sight equivalent hydrogen column density (N_H) of HMXBs. The X axis shows the out-of-eclipse to eclipse ratio of N_H, and the Y axis gives the out-of-eclipse to eclipse flux ratio. Here, the observation of 4U 1700−377 belongs to OBS ID: 0083280401.

differences in column density in the eclipse and out-of-eclipse phases.

Comparison of the fluxes in the 0.3–2.0 keV energy range in the eclipse and out-of eclipse phases indicates that the source of the soft excess is near the compact object in our sample of HMXBs, except in 4U 1538−522. In 4U 1538−522, the soft excess in both phases are comparable, which indicates that the soft excess must be originating far away from the system. The spectrum also softens during eclipse; perhaps the soft excess is due to dust scattering in the interstellar medium (ISM) along the line of sight. Robba et al. (2001) also observed a softening of the spectrum during total eclipse compared to the out-of-eclipse phase in 4U 1538−522; they suggest dust-scattering of the direct photon to be the origin of the soft excess in the

source. Audley et al. (2006) also found evidence of a dust halo surrounding the eclipsing HMXB OAO 1657−415.

3.5. Comparison of SFXTs and SgHMXBs

SFXTs have a much lower average X-ray luminosity compared to the SgHMXBs and only become bright during short flares. The compact objects in SFXTs are most probably neutron stars (in't Zand 2005). The SFXTs show a lower equivalent width of the Fe K_α emission line compared to SgHMXBs outside eclipse (Pradhan et al. 2018), with *Suzaku* and *XMM-Newton* data. Their findings in a large sample of both systems suggest that the compact object in the SFXT systems are surrounded by winds less dense than those in SgHMXBs. The compact object in SFXTs is inhibited from accreting from its companion most of the time (Sguera et al. 2005; Negueruela et al. 2006); the low-intensity X-ray emission is insufficient to reduce the speed of the supergiant's radiatively driven wind effectively. Hence, most of the wind passes by the compact object and is lost from the SFXT systems, and the compact objects in SFXTs are surrounded by less dense winds. Maccarone et al. (2014) suggested that some SFXTs might have an eccentric orbit, so the compact object spends most of the time away from its supergiant companion and hence is surrounded by less dense matter. But as a counterexample, indications of a circular orbit have been found in SFXT IGR J16479−4514, which has an orbital period of ∼3 days (Jain et al. 2009a; Sidoli et al. 2013). Considering a spherical wind outflow from the supergiant star and from the scattered and direct emission respectively during the eclipse and out-of-eclipse phases, an expected luminosity of these sources can be estimated, but it is two orders higher than the observed luminosity (Sidoli et al. 2013; Martínez-Núñez et al. 2017). The usual low luminosity in the SFXT systems can be explained if the neutron star remains in the supersonic propeller regime most of the time. This can lower the luminosity by a factor of 100–1000 compared to the case of direct accretion for neutron stars with spin period in the range of 10–100 s and magnetic field with $\mu_{30} = 0.1$–1 (Martínez-Núñez et al. 2017). If the interaction of the supergiant's wind with the compact object in these systems is very different from that in SgHMXBs, that could also make the compact object's environment less dense, which produces low equivalent widths of the Fe emission line (Pradhan et al. 2018).

However, the two SFXTs (IGR J16479−4514, IGR J16418−4532) in our sample have large Fe line equivalent widths comparable to those of the SgHMXBs during eclipses. IGR J16479−4514 and IGR J16418−4532 have equivalent widths of 803^{+89}_{-89} eV and 1358^{+453}_{-453} eV, respectively, for the fluorescent Fe K_α emission line during eclipses, while the equivalent width of this line for the SgHMXBs is in the range of (126–2695 eV). The equivalent widths of the Fe XXVI emission line are 576^{+345}_{-230} eV and 1911^{+1146}_{-764} eV, respectively, in the above two SFXTs. The line-of-sight hydrogen column density (N_H) in these SFXTs are like that of the other SgHMXBs in our sample. During eclipse, both the continuum and the Fe line are reprocessed emission from the same wind material, so a comparable equivalent width of the Fe line in SgHMXBs and SFXTs during eclipse only indicates similar Fe abundance in the two kinds of systems. A lower Fe abundance can possibly explain a lower line equivalent width in SFXTs outside the eclipse (as found by Pradhan et al. 2018), but such a possibility is ruled out with the current result. We need large samples with
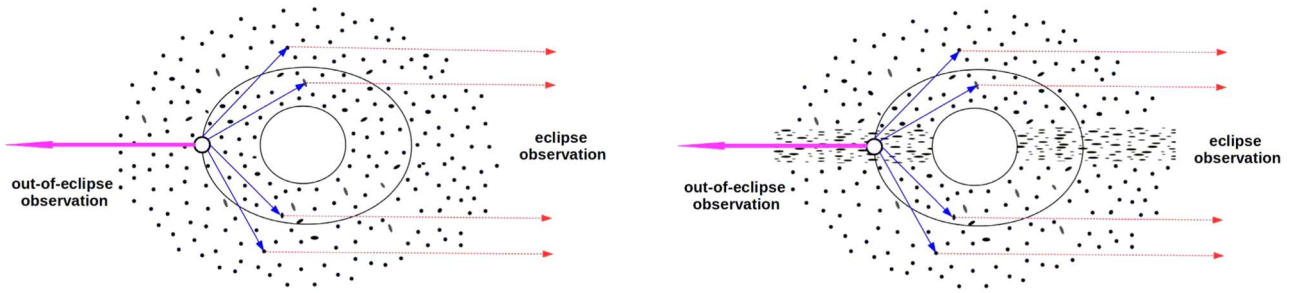
Figure 18. Probable distribution of wind around the neutron star in systems with a low ratio of the column density ($N_{\rm H}$) in the out-of-eclipse to the eclipse phase (left) and in systems in which this ratio of column densities is much larger (right). The small circle at the left of each figure represents the neutron star, and the bigger one represents the companion star. The primary and reprocessed X-rays are represented by solid and dashed arrows, respectively. The first system probably has a more isotropic wind pattern. A strong wind outflow in the equatorial or near-equatorial plane in the second system can explain the higher ratio of column densities between the out-of-eclipse to eclipse phase. During eclipse, the reprocessed X-rays represented by the dashed arrows reach the observer, and in both systems, it shows comparable $N_{\rm H}$. When the source is in the out-of-eclipse phase, the observer receives the direct X-rays, shown here in bold (pink) arrows. In the case of the first system during the out-of-eclipse phase, the observer looks through an isotropic wind as seen during eclipse. But for the second system during the out-of-eclipse phase, the direct X-rays reach the observer, penetrating dense wind.

multiple observations, during eclipses, to interpret the relation between the fluorescent Fe K_{α} emission line equivalent width and the luminosity and $N_{\rm H}$, and also to investigate the interaction of the compact object with the supergiant's wind and hence the wind distributions surrounding the compact objects in SFXTs.

4. Conclusion

We found ample diversity in the X-ray reprocessing characteristics in HMXBs. The out-of-eclipse to eclipse flux ratio was found to be in the range of $\sim$8–237, which implies significantly dynamic wind structure surrounding the compact object in HMXBs. Even in the same source at different epochs, the variation is quite large (86–237 in LMC X-4).

The equivalent widths of Fe emission lines found in SFXTs are large during eclipse, similar to those in SgHMXBs. The equivalent width of the fluorescent Fe K_{α} emission line found in the SFXTs IGR J16479$-$4514 and IGR J16418$-$4532 are 803^{+89}_{-89} eV and 1358^{+453}_{-453} eV, respectively, whereas the equivalent width of the Fe XXVI emission line was found to be 576^{+345}_{-230} eV and 1911^{+1146}_{-764} eV, respectively, in these two SFXTs. This implies a similar Fe-rich medium in SFXTs, like in SgHMXBs.

Cen X-3 is one exception for which the equivalent width of the Fe K_{α} emission line is lower during eclipse compared to the out-of-eclipse phase; this indicates an Fe-rich, dense accretion disk or accretion stream near the compact object.

In 4U 1538$-$522, the soft X-ray emission flux is nearly the same in the out-of-eclipse and eclipse phases, i.e., the soft X-ray emission is not blocked during the eclipse of the compact object by the supergiant companion, which clearly indicates a different origin for the hard and soft X-rays. Perhaps dust scattering of the direct photons in ISM, far away from the source, is the origin of this soft excess.

Some systems show comparable wind density near and far away from the compact object (Cen X-3, LMC X-4, SMC X-1). There are some indications of equatorial or near-equatorial dense wind outflows from the supergiant in three different observations (IGR J18027$-$2016, 4U 1538$-$522, and the first observation of 4U 1700$-$377).

ORCID iDs

Peter Kretschmar https://orcid.org/0000-0001-9840-2048

References

Aftab, N., Islam, N., & Paul, B. 2016, MNRAS, 463, 2032
Ankay, A., Kaper, L., de Bruijne, J. H. J., et al. 2001, A&A, 370, 170
Ash, T. D. C., Reynolds, A. P., Roche, P., et al. 1999, MNRAS, 307, 357
Audley, M. D., Nagase, F., Mitsuda, K., Angelini, L., & Kelley, R. L. 2006, MNRAS, 367, 1147
Augello, G., Iaria, R., Robba, N. R., et al. 2003, ApJL, 596, L63
Barthelmy, S. D., Barbier, L. M., Cummings, J. R., et al. 2005, SSRv, 120, 143
Becker, R. H., Swank, J. H., Boldt, E. A., et al. 1977, ApJL, 216, L11
Beri, A., & Paul, B. 2017, NewA, 56, 94
Bildsten, L., Chakrabarty, D., Chiu, J., et al. 1997, ApJS, 113, 367
Blondin, J. M. 1994, ApJ, 435, 756
Bozzo, E., Giunta, A., Stella, L., et al. 2009, A&A, 502, 21
Burderi, L., Di Salvo, T., Robba, N. R., La Barbera, A., & Guainazzi, M. 2000, ApJ, 530, 429
Clark, J. S., Goodwin, S. P., Crowther, P. A., et al. 2002, A&A, 392, 909
Coe, M. J., Burnell, S. J. B., Engel, A. R., Evans, A. J., & Quenby, J. J. 1981, MNRAS, 197, 247
Coleiro, A., Chaty, S., Zurita Heras, J. A., Rahoui, F., & Tomsick, J. A. 2013, A&A, 560, A108
Coley, J. B., Corbet, R. H. D., & Krimm, H. A. 2015, ApJ, 808, 140
Corbet, R., Barbier, L., Barthelmy, S., et al. 2006, ATel, 779
Corbet, R. H. D., & Krimm, H. A. 2013, ApJ, 778, 45
Day, C. S. R., & Stevens, I. R. 1993, ApJ, 403, 322
de Jong, J. A., van Paradijs, J., & Augusteijn, T. 1996, A&A, 314, 484
del Sordo, S., dal Fiume, D., Oriandini, M., et al. 2000, AdSpR, 25, 413
Drave, S. P., Bird, A. J., Goossens, M. E., et al. 2013a, ATel, 5131
Drave, S. P., Bird, A. J., Sidoli, L., et al. 2013b, MNRAS, 433, 528
Ebisawa, K., Day, C. S. R., Kallman, T. R., et al. 1996, PASJ, 48, 425
Falanga, M., Bozzo, E., Lutovinov, A., et al. 2015, A&A, 577, A130
Gehrels, N., Chincarini, G., Giommi, P., et al. 2004, ApJ, 611, 1005
George, I. M., & Fabian, A. C. 1991, MNRAS, 249, 352
Giacconi, R., Gursky, H., Kellogg, E., Schreier, E., & Tananbaum, H. 1971, ApJL, 167, L67
Gierliński, M., Done, C., & Page, K. 2009, MNRAS, 392, 1106
Giménez-García, A., Torrejón, J. M., Eikmann, W., et al. 2015, A&A, 576, A108
Guainazzi, M., Kirsch, M., Haberl, F., et al. 2014, Spectral Calibration Accuracy in EPIC-pn Fast Modes XMM-Newton Calibration Tech. Note XMM-SOC-CAL-TN-0083 (Paris: ESA), http://xmm.vilspa.esa.es/docs/documents/CAL-TN-0083.pdf

Haberl, F., Aoki, T., & Mavromatakis, F. 1994, A&A, 288, 796
Haberl, F., & Day, C. S. R. 1992, A&A, 263, 241
Hemphill, P. B., Rothschild, R. E., Cheatham, D. M., et al. 2019, ApJ, 873, 62
Hemphill, P. B., Rothschild, R. E., Markowitz, A., et al. 2014, ApJ, 792, 14
Hickox, R. C., & Vrtilek, S. D. 2005, ApJ, 633, 1064
Hilditch, R. W., Howarth, I. D., & Harries, T. J. 2005, MNRAS, 357, 304
Hill, A. B., Walter, R., Knigge, C., et al. 2005, A&A, 439, 255
Hu, C.-P., Chou, Y., Yang, T.-C., & Su, Y.-H. 2013, ApJ, 773, 58
Hung, L.-W., Bañados, E., De Propris, R., & West, M. J. 2010, ApJ, 720, 1483
in't Zand, J. J. M. 2005, A&A, 441, L1
Islam, N., & Paul, B. 2014, MNRAS, 441, 2539
Islam, N., & Paul, B. 2016, MNRAS, 461, 816
Jain, C., Paul, B., & Dutta, A. 2009a, MNRAS, 397, L11
Jain, C., Paul, B., & Dutta, A. 2009b, RAA, 9, 1303
Jaisawal, G. K., & Naik, S. 2015, MNRAS, 448, 620
Jethwa, P. 2012, Pile-up Thresholds for the EPIC Cameras, XMM-Newton Calibration Tech. Note CAL-TN-0200-1-0 (Paris: ESA), http://xmm2.esac.esa.int/docs/documents/CAL-TN-0200-1-0.pdf
Jones, C., Forman, W., Tananbaum, H., et al. 1973, ApJL, 181, L43
Kaastra, J. S., & Mewe, R. 1993, A&AS, 97, 443
Kirsch, M. G. F., Schönherr, G., Kendiorra, E., et al. 2006, A&A, 453, 173
Krimm, H. A., Holland, S. T., Corbet, R. H., et al. 2013, ApJS, 209, 14
Kubota, M., Odaka, H., Tamagawa, T., & Nakano, T. 2018, ApJL, 868, L26
Lang, F. L., Levine, A. M., Bautz, M., et al. 1981, ApJL, 246, L21
Levine, A., Rappaport, S., Deeter, J. E., Boynton, P. E., & Nagase, F. 1993, ApJ, 410, 328
Levine, A. M., Rappaport, S. A., & Zojcheski, G. 2000, ApJ, 541, 194
Li, F., Rappaport, S., & Epstein, A. 1978, Natur, 271, 37
Liu, Q. Z., van Paradijs, J., & van den Heuvel, E. P. J. 2000, A&AS, 147, 25
Lumb, D. H., Schartel, N., & Jansen, F. A. 2012, Opt. Eng., 51, 011009
Lutovinov, A. A., Tsygankov, S. S., Postnov, K. A., et al. 2017, MNRAS, 466, 593
Maccarone, T. J., Girard, T. M., & Casetti-Dinescu, D. I. 2014, MNRAS, 440, 1626
Manousakis, A., & Walter, R. 2011, A&A, 526, A62
Martínez-Núñez, S., Kretschmar, P., Bozzo, E., et al. 2017, SSRv, 212, 59
Martins, F., Schaerer, D., & Hillier, D. J. 2005, A&A, 436, 1049
Mason, K. O., Breeveld, A., Much, R., et al. 2001, A&A, 365, L36
Molkov, S., Mowlavi, N., Goldwurm, A., et al. 2003, ATel, 176
Moon, D.-S., Eikenberry, S. S., & Wasserman, I. M. 2003, ApJ, 586, 1280
Mukherjee, U., Raichur, H., Paul, B., Naik, S., & Bhatt, N. 2006, JApA, 27, 411
Nagase, F., Corbet, R. H. D., Day, C. S. R., et al. 1992, ApJ, 396, 147
Naik, S., & Paul, B. 2004a, A&A, 418, 655
Naik, S., & Paul, B. 2004b, ApJ, 600, 351
Naik, S., & Paul, B. 2012, BASI, 40, 503
Naik, S., Paul, B., & Ali, Z. 2011, ApJ, 737, 79
Negueruela, I., Smith, D. M., Reig, P., Chaty, S., & Torrejón, J. M. 2006, ESASP, 604, 165
Neilsen, J., Lee, J. C., Nowak, M. A., Dennerl, K., & Vrtilek, S. D. 2009, ApJ, 696, 182
Nespoli, E., Fabregat, J., & Mennickent, R. E. 2008, A&A, 486, 911
Oskinova, L. M., Feldmeier, A., & Kretschmar, P. 2013, in IAU Symp. 290, Feeding Compact Objects: Accretion on All Scales, ed. C. M. Zhang et al. (Cambridge: Cambridge Univ. Press), 287
Parkes, G. E., Murdin, P. G., & Mason, K. O. 1978, MNRAS, 184, 73P
Paul, B., & Kitamoto, S. 2002, JApA, 23, 33
Penny, A. J., Olowin, R. P., Penfold, J. E., & Warren, P. R. 1973, MNRAS, 163, 7P
Pietrzyński, G., Graczyk, D., Gieren, W., et al. 2013, Natur, 495, 76
Pike, S. N., Harrison, F. A., Bachetti, M., et al. 2019, ApJ, 875, 144
Pradhan, P., Bozzo, E., & Paul, B. 2018, A&A, 610, A50
Price, R. E., Groves, D. J., Rodrigues, R. M., et al. 1971, ApJL, 168, L7

Primini, F., Rappaport, S., & Joss, P. C. 1977, ApJ, 217, 543
Raichur, H., & Paul, B. 2010, MNRAS, 401, 1532
Reynolds, A. P., Bell, S. A., & Hilditch, R. W. 1992, MNRAS, 256, 631
Reynolds, A. P., Hilditch, R. W., Bell, S. A., & Hill, G. 1993, MNRAS, 261, 337
Robba, N. R., Burderi, L., Di Salvo, T., Iaria, R., & Cusumano, G. 2001, ApJ, 562, 950
Rodes-Roca, J. J., Page, K. L., Torrejón, J. M., Osborne, J. P., & Bernabéu, G. 2011, A&A, 526, A64
Romano, P., Sidoli, L., Cusumano, G., et al. 2009, MNRAS, 399, 2021
Romano, P., Sidoli, L., Mangano, V., et al. 2008, ApJL, 680, L137
Romano, P., Mangano, V., Ducci, L., et al. 2012, MNRAS, 419, 2695
Romano, P., Mangano, V., Esposito, P., et al. 2011, ATel, 3174
Sako, M., Liedahl, D. A., Kahn, S. M., & Paerels, F. 1999, ApJ, 525, 921
Santangelo, A., del Sordo, S., Segreto, A., et al. 1998, A&A, 340, L55
Savonije, G. J. 1978, A&A, 62, 317
Schreier, E., Giacconi, R., Gursky, H., Kellogg, E., & Tananbaum, H. 1972a, ApJL, 178, L71
Schreier, E., Levinson, R., Gursky, H., et al. 1972b, ApJL, 172, L79
Schulz, N. S., Canizares, C. R., Lee, J. C., & Sako, M. 2002, ApJL, 564, L21
Sguera, V., Barlow, E. J., Bird, A. J., et al. 2005, A&A, 444, 221
Shtykovsky, A. E., Arefiev, V. A., Lutovinov, A. A., & Molkov, S. V. 2018, AstL, 44, 149
Sidoli, L., Esposito, P., Sguera, V., et al. 2013, MNRAS, 429, 2763
Sidoli, L., Mereghetti, S., Sguera, V., et al. 2012b, in Proc. An INTEGRAL View of the High-energy Sky (the First 10 years), 9th INTEGRAL Workshop and Celebration of the 10th Anniversary of the Launch (INTEGRAL 2012), 34, http://pos.sissa.it/cgi-bin/reader/conf.cgi?confid=176
Sidoli, L., Mereghetti, S., Sguera, V., & Pizzolato, F. 2012a, MNRAS, 420, 554
Sidoli, L., Romano, P., Mangano, V., et al. 2008, ApJ, 687, 1230
Strüder, L., Briel, U., Dennerl, K., et al. 2001, A&A, 365, L18
Suleimanov, V., Meyer, F., & Meyer-Hofmeister, E. 2003, A&A, 401, 1009
Takeuchi, Y., Koyama, K., & Warwick, R. S. 1990, PASJ, 42, 287
Tawara, Y., Yamauchi, S., Awaki, H., et al. 1989, PASJ, 41, 473
Thompson, T. W. J., & Rothschild, R. E. 2009, ApJ, 691, 1744
Thompson, T. W. J., Tomsick, J. A., in 't Zand, J. J. M., Rothschild, R. E., & Walter, R. 2007, ApJ, 661, 447
Torrejón, J. M., Negueruela, I., Smith, D. M., & Harrison, T. E. 2010a, A&A, 510, A61
Torrejón, J. M., Schulz, N. S., Nowak, M. A., & Kallman, T. R. 2010b, ApJ, 715, 947
Turner, M. J. L., Abbey, A., Arnaud, M., et al. 2001, A&A, 365, L27
Ulmer, M. P., Baity, W. A., Wheaton, W. A., & Peterson, L. E. 1973, NPhS, 242, 121
Vacca, W. D., Garmany, C. D., & Shull, J. M. 1996, ApJ, 460, 914
Val Baker, A. K. F., Norton, A. J., & Quaintrell, H. 2005, A&A, 441, 685
van der Meer, A., Kaper, L., di Salvo, T., et al. 2005, A&A, 432, 999
van der Meer, A., Kaper, L., van Kerkwijk, M. H., Heemskerk, M. H. M., & van den Heuvel, E. P. J. 2007, A&A, 473, 523
Varun, M. C., Pradhan, P., Raichur, H., & Paul, B. 2019, MNRAS, 484, L1
Walter, R., Bodaghee, A., Barlow, E. J., et al. 2004, ATel, 229
Walter, R., & Zurita Heras, J. 2007, A&A, 476, 335
Walter, R., Zurita, H., Bassani, L., et al. 2006, A&A, 453, 133
Weaver, K. A., Nousek, J., Yaqoob, T., et al. 1996, ApJ, 458, 160
White, N. E. 1978, Natur, 271, 38
White, N. E., Kallman, T. R., & Swank, J. H. 1983, ApJ, 269, 264
Wojdowski, P., Clark, G. W., Levine, A. M., Woo, J. W., & Zhang, S. N. 1998, ApJ, 502, 253
Wojdowski, P. S., Liedahl, D. A., & Sako, M. 2001, ApJ, 547, 973
Woo, J. W., Clark, G. W., Levine, A. M., Corbet, R. H. D., & Nagase, F. 1996, ApJ, 467, 811
Zurita Heras, J. A., De Cesare, G., Walter, R., et al. 2006, A&A, 448, 261
Zycki, P. T., Krolik, J. H., Zdziarski, A. A., & Kallman, T. R. 1994, ApJ, 437, 597